REVISION 2 correction date 03/11/2020

Characterization and assessment of the potential toxicity/pathogenicity of Russian commercial chrysotile

DARIO DI GIUSEPPE[1,2,*], ALESSANDRO ZOBOLI[1], LUCA NODARI[3], LUCA PASQUALI[4], ORIETTA SALA[1], PAOLO BALLIRANO[5], DANIELE MALFERRARI[1], SIMONA RANERI[6], MIRIAM HANUSKOVA[4], AND ALESSANDRO F. GUALTIERI[1]

[1]Department of Chemical and Geological Sciences, University of Modena and Reggio Emilia, Via G. Campi 103, Modena, I-41125, Italy.
[2]Department of Sciences and Methods for Engineering, University of Modena and Reggio Emilia, Via Amendola 2, Reggio Emilia, I-42122, Italy.
[3]ICMATE-CNR, Institute of Condensed Matter Chemistry and Technologies for Energy, Italian National Research Council, Corso Stati Uniti 4, I-35127, Padova, Italy.
[4]Department of Engineering "Enzo Ferrari", University of Modena and Reggio Emilia, Via Pietro Vivarelli 10, I-41125, Modena, Italy.
[5]Department of Earth Sciences, Sapienza University of Rome, Piazzale Aldo Moro 5, I-00185, Rome, Italy.
[6]ICCOM-CNR, Institute of Chemistry of Organometallic Compounds, Italian National Research Council, Via G. Moruzzi 1, I-56124, Pisa, Italy.
* Corresponding author, e-mail address: ddigiuse@unimore.it, Tel. +390592058497

ABSTRACT

Today, cancer is one of the main health issues faced in the workplace with asbestos an important carcinogen in the occupational environment. Among the asbestos minerals, chrysotile is the main species of socio-economic and industrial relevance. Although chrysotile asbestos is classified as a "carcinogenic substance" by the International Agency for Research on Cancer (IARC), this fiber is still mined and used in Russia. The effective health hazard posed by the Russian commercial chrysotile has not been quantitatively assessed to date. In this work, the potential toxicity/pathogenicity of Russian chrysotile was quantitatively determined using the fiber potential toxicity index (FPTI) model. This model was applied to a representative commercial chrysotile from the Orenburg region, Russia, whose morphometric, crystal-chemical, surface activity and biodurability related parameters were determined. We have quantitatively assessed that the toxicity/pathogenicity potential of Russian chrysotile (FPTI = 2.4) is lower than that of amphibole asbestos species but higher than the threshold limit set for “safe” mineral fibers (FPTI = 2.0), although it does not contain impurities of amphibole asbestos. Differences with other chrysotile samples were discussed and it was found that the investigated Russian commercial chrysotile shares several features with the Italian Balangero chrysotile, indicating that widespread concern on commercial Russian chrysotile is justified.

Keywords: Asbestos; Chrysotile; Russia; Adverse Effects; FPTI.

This is the peer-reviewed, final accepted version for American Mineralogist, published by the Mineralogical Society of America.
The published version is subject to change. Cite as Authors (Year) Title. American Mineralogist, in press.
DOI: https://doi.org/10.2138/am-2021-7710. http://www.minsocam.org/

INTRODUCTION

Chrysotile is a trioctahedral hydrous layer silicate with ideal chemical formula $Mg_3(OH)_4Si_2O_5$. Together with lizardite and antigorite, chrysotile belongs to the serpentine group. Its basic structure is composed of one Mg-centered octahedral sheet (O) covalently bonded to one Si-centered tetrahedral sheet (T) (Ballirano et al. 2017). The lateral size of an ideal Mg-centered O sheet is larger than the lateral size of an ideal Si-centered T sheet. The dimensional misfit causes a differential stress that is mostly released by rolling the TO layers into a tubular structure providing chrysotile its characteristic fibrous habit (Ballirano et al. 2017). Because of its fibrous crystal habit and outstanding physical-chemical properties, chrysotile is the most common asbestos mineral on Earth (Gualtieri 2012).

Asbestos is actually a commercial term designating six mineral fibers used for industrial applications: chrysotile and the five amphiboles actinolite asbestos, amosite (fibrous variety of cummingtonite-grunerite), anthophyllite asbestos, crocidolite (fibrous variety of riebeckite) and tremolite asbestos (NIOSH 2011; IARC 2012). Asbestos minerals have been used in the human history to create more than 3000 asbestos-containing materials (ACM), such as electrical and thermal insulating materials (flooring and coatings), vinyl-asbestos, asbestos-cement roofs and pipes (Ross and Nolan 2003; Gualtieri 2017). Extensive use of asbestos began in the 19th century when mine mechanization promoted the exploitation of large chrysotile deposits in Canada (e.g., Lake Asbestos, Quebec) and Europe (e.g., Balangero mine, Italy). Modernization of the rail network enabled the intensive exploitation of the Uralasbest mine in Russia (Vogel 2005; Marsili 2007). In 1975, Russia became the world's leading asbestos producer and it is still so today (Kashansky et al. 2001; USGS 2020). In the last century, about 30 million tons of asbestos fibers have been mined worldwide and about 90% of this raw material is chrysotile (LaDou 2004; WHO 2014). Regrettably, since the beginning of the 20th century, it has become clear that the unique crystal-chemical and physical features of asbestos minerals, responsible for their exceptional properties, are related to potential pathogenicity

(Gualtieri 2017). Sir Richard Doll for the first time unequivocally reported the link between lung cancer and asbestos fibers inhalation in a cohort of workers exposed to asbestos (Doll 1955). Later, numerous cohort and case control studies have demonstrated the association between asbestos exposure and occupational cancers (IARC 2012). Meanwhile, from 1970 to 2000s, several studies used animal models to evaluate the carcinogenic potential of asbestos fibers. These contributions were summarized by the Working Group of the International Agency for Research on Cancer (IARC) in Monograph 100c, containing all epidemiological and carcinogenicity studies conducted to that date (IARC 2012). In the Monograph 100c, an IARC Working Group concluded that there is enough scientific evidence that all asbestos species can cause malignant mesothelioma (MM) and cancer of the lung, larynx and ovary. Hence, all forms of asbestos (i.e., chrysotile and amphibole asbestos) have been classified by the IARC as carcinogenic to humans (*Group 1*). Concurrently, starting from the 80s, many European countries banned asbestos. Today, 67 countries including Canada, Italy, South Africa, United Kingdom and Japan have banned all asbestos minerals (IBAS 2020). Amphibole asbestos is rarely mined today (Ilgren et al. 2015) whereas chrysotile asbestos is still largely used in about 65% of the countries worldwide including China, India, Kazakhstan, and Russia (IBAS 2020). These countries allow the so-called "safe use" (i.e., its manipulation wearing individual protection devices) of chrysotile, assuming that low exposures to chrysotile do not present a detectable risk to health and that, if compared to amphibole asbestos, chrysotile is less potent for the induction of lung cancer and MM (Camus 2001; Bernstein et al. 2013). This model is based on the different biopersistence of chrysotile with respect to amphibole asbestos. Biopersistence is the ability of an exogenous particle (such as an asbestos fiber) to persist in the human body regardless of chemical dissolution (biodurability) and physical clearance mechanisms (Bernstein et al. 2005). During the process of phagocytosis by alveolar macrophages *in vivo*, the acid environment produced intracellularly attacks chrysotile fibers that rapidly undergo a process of dissolution, with leaching of Mg and production of amorphous silica relicts (Gualtieri et al.

2019a) which is eliminated by macrophages (Bernstein et al. 2013). On the other hand, amphibole asbestos fibers are biodurable (Bernstein et al. 2005; 2013) and induce chronic inflammation responsible for adverse effects *in vivo* (Bernstein et al. 2014; 2015; Bernstein and Pavlisko 2017). This model is not universally accepted as biodurability alone cannot explain the toxicity and pathogenicity of mineral fibers. As a matter of fact, a vast part of the scientific community and government authorities support the model that all asbestos minerals are toxic and pathogenic and all increase the risk of MM (Collegium Ramazzini 2010).

The chrysotile debate is an open issue mostly because the mechanisms by which asbestos fibers induce adverse effects on human health are still not fully understood (Gualtieri et al. 2017). The difficulties stem from the fact that asbestos-related carcinogenesis is the results of a complex multistep process and assessing the potential toxicity/pathogenicity of a mineral fiber is a tangled task. It is important to remark that the adverse effects induced *in vivo* by asbestos, in addition to the fibers' biodurability, depend on its chemical composition, crystal structure, surface properties and morphology, as well as on the load of fibers (IARC 2012; Gualtieri et al. 2017). To objectively and quantitatively compare the hazard represented by the different mineral fibers and especially chrysotile and amphibole asbestos, Gualtieri (2018) recently proposed a quantitative predictive model of toxicity/pathogenicity of minerals fibers based on the physical/chemical and morphological parameters that affect the biological activity. This model delivers an index (FPTI) aimed at ranking the toxicity and pathogenicity of mineral fibers (Gualtieri 2018; Mossman and Gualtieri 2020). To calculate FPTI, the model considers all the parameters that induce toxicity/pathogenicity, i.e., morphometric, chemical, biodurability related, and surface activity related parameters (Gualtieri 2018; Di Giuseppe et al. 2019; Mossman and Gualtieri 2020). In the work of Gualtieri (2018) a difference in the toxicity/pathogenicity potential of amphibole asbestos compared to chrysotile asbestos was highlighted based on their FPTI. In fact, the calculated mean value of FPTI of the amphibole asbestos family is significantly higher than

that of a suite of chrysotile asbestos samples (Gualtieri 2018). Moreover, the mean FPTI of chrysotile is significantly higher than the threshold limit set for `safe` mineral fibers such as wollastonite and sepiolite (Gualtieri 2018).

The last report on Asbestos Statistics and Information delivered by the United States Geological Service (USGS) shows that the world total mine production of chrysotile asbestos for 2019 was 1,100,000 tons (USGS 2020) and the main chrysotile producer in the world is Russia (750,000 tons/year). Russia's chrysotile resources (110×10^3 tons) occur in the Urals Mountains and are estimated to be adequate to meet the demand of the global asbestos market in the near future (USGS 2020). In this scenario, the active chrysotile mines of the Urals represent an important source of exposure to asbestos fibers. This situation causes great concern due to the dust generated by the excavation activities that may potentially expose workers and the local residents (Kashansky et al. 2001). Furthermore, it should be considered that Russian chrysotile is largely used in the Russian internal market and exported to all the countries where asbestos is not banned such as China and India, exposing their work forces and populations (Burkhanova et al. 2019). Although some studies were published (Tossavainen et al. 2000; Kanarek 2011; Kovalevskiy et al. 2016; Schüz et al. 2013; 2020), the effective potential toxicity/pathogenicity of Russian chrysotile has not been quantitatively assessed.

In the present study a detailed characterization of Russian commercial chrysotile is presented and the FPTI model (Gualtieri 2018; Mossman and Gualtieri 2020) is applied with the aim of contributing to the global chrysotile issue. The calculated FPTI was compared to that of amphibole asbestos fibers and well-characterized chrysotiles: 1) Union for International Cancer Control (UICC) standard chrysotile asbestos “B” Canadian (NB #4173-111-1) from Quebec, Canada; 2) chrysotile asbestos from Balangero (Turin, Italy); and 3) chrysotile asbestos from Valmalenco (Sondrio, Italy).

SOURCE OF THE SAMPLE AND GEOLOGICAL OVERVIEW

A commercial sample of chrysotile from Orenburg Minerals mine near Yasniy, Russia, has been investigated. The chrysotile fibers from Yasniy are sold in bags of a net weight of 25 or 50 kg. This raw material is commonly used as a reinforcing and thermal insulating agent. It is also employed for the production of asbestos-cement products (e.g., pipes, sheets and shingles), as a granular stabilizer of asphalt, as heat insulation in the form of cords and a cardboard, as thermal insulation of furnaces and lining of steam boilers, and in the form of sealants in devices affected by high temperatures.

Yasniy (Russian: Я́сный; which means clear) is a town located in the Orenburg region, southern Ural Mountains, near the border between Russia and Kazakhstan (Fig. 1a). Complete description of the geological features of the Urals and geodynamic processes that characterized the tectonics of this area can be found in Ivanov et al. (2013) and Puchkov (2017). The Urals are an orogenic belt which ideally forms the boundary between Europe and Asia. The Uralian belt extends 2500 km from the Polar Urals to the Aral Lake along the 60° East Meridian (Fig. 1a). It was formed by a Paleozoic continental collision subsequent to the closure of a pre-Paleozoic ocean located between the European and Siberian-Kazakh plates (Ivanov and Rusin 1986; Garuti et al. 2012). The Urals are conventionally divided into various geotectonic units, extending continuously from north to south and broadly parallel to the Main Uralian Fault (MUF) that represents the westernmost and principal tectonic boundary between the abovementioned collided plates (Ivanov et al. 2013; Garuti et al. 2012). A simplified scheme of Urals geotectonic units is presented in Figure 1b and includes the followings from west to east (Shahgedanova 2003; Ivanov et al. 2013; Garuti et al. 2012; Puchkov 2017):

A) Pre-Uralian foredeep (pre-flysch deep-water condensed sediments, flysch, evaporites and molasse of the Upper Paleozoic and partly Triassic age);

B) West-Uralian zone (paleoshelf terrigenous carbonate series and terrigenous-siliceous-shale deposits, dated from Ordovician to Carboniferous);

C) Central-Uralian zone (metamorphosed Precambrian and Early Paleozoic rocks);

D) The Suture-zone and Tagil-Magnitogorsk-zone, limited from the west by the MUF, consist of a succession of Paleozoic oceanic lithosphere (ophiolites) and island arc formations,

E) East Uralian zone, containing a combination of Precambrian and Paleozoic oceanic and island arc complexes

F) Trans-Uralian zone, composed of pre-Carboniferous complexes, probably accretionary in origin, unconformably covered by the Lower Carboniferous calc-alkaline volcanic rocks.

The rocks extracted at the Yasniy mine are serpentinized ophiolites (Fig. 1c) that belong to geotectonic units D) which include the Suture-zone and Tagil-Magnitogorsk-zone (Gannoun et al. 2003). In particular, the mine is located on an ophiolite massifs 90 km east of the city of Orsk, Orenburg Region (Fig. 1c). Ophiolite massifs of this area belong to the Sakmarsko–Khalilovsky group, i.e., a wide ophiolite complex composed of serpentine derived from harzburgite and dunite (Gannoun et al. 2003). Chrysotile is hosted in the serpentinized rock together with lizardite and minor clay minerals, dolomite, calcite, magnesite and magnetite (Khilyas et al. 2019).

ANALYTICAL METHODS

Sample grinding

Several analytical procedures used for the characterization of Yasniy chrysotile require sample milling. This is rather complicated as conventional grinding techniques have modest if any effect on chrysotile fibers (Pollastri et al. 2016a). For this reason, we have opted for cryo-milling at dry conditions, using a Resch mixer mill MM 400 (Düsseldorf, Germany) equipped with steel grinding balls and steel jars, coated with polytetrafluoroethylene (PTFE). PTFE prevents the contamination of sample from iron and other metals released by the steel. The jars were first filled with the sample and the grinding balls, soaked in liquid nitrogen until reaching the temperature of -196 °C, then mounted in

the mill. The milling time was variable depending on the amount of sample but always in the order of few minutes.

X-ray powder diffraction (XRPD)

XRPD data were collected in the 7-145 °2θ, step size 0.022 °2θ, 8 s/step, using a Bruker AXS D8 Advance diffractometer (Karlsruhe, Germany). The instrument operates in θ/θ geometry, in transmission mode, and is equipped with Göbel mirrors on the incident beam, Soller slits on both incident and (radial) diffracted beams, and a PSD VÅNTEC-1 detector. The sample was prepared following the same procedure reported in Cametti et al. (2013) for woolly erionite from Durkee. Bundles of fibers were selected and disaggregated under a binocular microscope using a knife. Subsequently, they were carefully hand-ground in an agate mortar under ethanol in order to increase disaggregation. Upon drying, the resulting material consisting of small flakes of randomly intersecting fibers, was loaded into a 1 mm diameter borosilicate capillary that was aligned onto a standard goniometer head. Phase identification was performed with the DIFFRAC.EVA V5.1 software (Bruker AXS 2019) using the ICDD PDF 2 reference database for mineral phases (ICDD 2020).

Electron Microscopy

Detailed observation of the sample was performed using a Field Emission Gun (FEG) Scanning Electron Microscope (SEM), FEI Nova NanoSEM 450 FEG-SEM (Hillsboro, OR, USA) equipped with an Energy Dispersive X-ray (EDX) spectrometer. Operating conditions were 15 kV accelerating voltage, 3.5 μA emission current, 20 nA beam current and 6 mm working distance. An aliquot of raw sample was suspended in distilled water and fixed on an aluminum stub with double-stick carbon tape, left to dry and then sputter-coated with gold (10 nm of thickness), using a gold sputter coater - Emitech K550 (London, UK). Images were acquired using secondary electrons. EDX spectra were always collected to confirm the chemical nature of the mineral fibers. A surface of 1 mm^2 was investigated, collecting 200 random fields at 2000× and down to 10,000× for the morphometric characterization. The

This is the peer-reviewed, final accepted version for American Mineralogist, published by the Mineralogical Society of America.
The published version is subject to change. Cite as Authors (Year) Title. American Mineralogist, in press.
DOI: https://doi.org/10.2138/am-2021-7710. http://www.minsocam.org/

size and morphometric parameters of the single fibers were determined on 200 individuals. Lengths and widths were calculated using ImageJ image analysis software, version 1.52a (NIMH 2018).

The sample was also observed using transmission electron microscope (TEM). TEM investigations were carried out using a Talos F200S G2 microscope (Thermo Fisher Scientific, Waltham, USA), equipped with S-FEG Schottky field emitter operating at 200 kV and two large-area energy-dispersive X-ray (EDX) spectrometers with Silicon Drift Detectors (SDD). A small amount of sample was suspended with 1 mL of ethanol in a test tube, sonicated for 20 min (using a low power sonic bath) and left to set for 5 min. Then, a drop of the suspension was transferred onto a 300-mesh carbon copper TEM grid (Ted Pella Inc., Redding, USA) and left to dry. Observations were made both in TEM and Scanning TEM (STEM) mode.

Optical microscopy

The optical properties of chrysotile fibers were determined using polarized light and chromatic dispersion techniques. Phase Contrast Optical Microscopy (PCOM) with chromatic dispersion is a fast-qualitative analysis that allows the identification of nature of a mineral fiber from its chromatic dispersion (Cavariani et al. 2010; Gualtieri et al. 2018a). PCOM analysis is based on the optical principle that mineral fibers placed in specific high-dispersion liquids, show typical chromatic effects that allow their identification (Baietto and Marini 2018). Cargille Refractive Index Liquid n = 1.550 was used for the identification of chrysotile. PCOM analyses were conducted following the methodology of Gualtieri et al. (2018a). Two drops of refractive index medium were placed on a pre-cleaned glass slide (76×26 mm). A small amount of sample was transferred to the slide. A coverslip was placed on the suspension and manually pressed to homogenize the distribution of the fibers on the slide and avoid bubbles. A Leica DM4000 B LED (Hüllhorst, Germany) equipped with Leica objectives (magnifications 10x, 20x, and 40x) was used for the dispersion staining observations. A

Leica D-LUX 3 digital camera was used for image collection. Image magnification was calibrated using a 1 mm stage micrometer with 100 increments of 0.1 mm.

Polarized Light Optical Microscopy (PLOM) was performed in transmitted light with an Olympus CHA (Tokyo, Japan) polarizing light microscope equipped with: 4×, 10×, 20× and 40× objective lenses, 6 V and 10 W halogen light source, 360° circular rotating stage and first order red quarter wavelength compensator plate. A small amount of sample was embedded in epoxy resin and fixed to a glass slide. The sample was subsequently lapped to a thickness of 30 μm.

Determination of the specific surface area (SSA)

SSA of the sample was determined using the BET-method (Brunauer et al. 1938). The SSA analyses were carried out using a Gemini V instrument (Micromeritics) with nitrogen as probe gas. About 300 mg of sample dehydrated at 100 °C for 24 h was mounted in the sample holder and conditioned at 50 °C prior to measurement. The analysis was carried out using liquid nitrogen cooled to -196 °C. Measurements were conducted with an equilibration time of 10 s and a saturation pressure of 777.28 mmHg.

Determination of the zeta potential

The zeta potential of the sample was determined using a Zetasizer Nano Series instrument (Malvern, Worcestershire, UK). Analyses were performed using double-distilled water and artificial lysosomal fluid (ALF) solution (pH=4) (Marques et al. 2011; Pollastri et al. 2014; Gualtieri et al. 2018b). The latter was used to simulate the lysosomal environment (Marques et al. 2011; Gualtieri et al. 2018b). Sample powder was added to the dispersants in a weight percentage of 0.1% and subjected to ultrasonic treatment for 15 min. Zeta potential measurements were conducted at a temperature of 37 °C, equilibration time of 120 s and different pH (from 2 to 10). A few drops of HCl 1N were added to the suspension to obtain a pH of 2. The pH was then raised up to 10 using NaOH 0.1 N. The pH was

monitored using a HANNA edge pH-meter (Woonsocket, USA). Zeta potential measurements were collected three times for each sample to check the reproducibility of the results.

Determination of density and aerodynamic diameter

Density (ρ) of the Yasniy chrysotile was measured using the pycnometer AccuPyc II 1340 Micromeritics (Georgia, USA) following the methodology of Di Giuseppe et al. (2014). The pycnometer uses the gas displacement method to measure volume of solid or powdered objects of known weight. Dividing the weight of the sample by the calculated volume yields the ρ of the sample. The weight of sample was measured using a Mettler Toledo (Ohio, USA) analytical scale. Helium with a total purity > 99.999% mol was used as dispersion medium. Chrysotile fibers were sealed in the pycnometer sample holder of known volume, an appropriate helium volume was injected, and then expanded into another precision internal volume. Helium molecules rapidly fill pores as small as 1 Å in diameter; only the solid phase of the sample displaces the gas. The pressures observed upon filling the sample chamber and then discharging it into a second empty chamber allow computation of the sample solid phase volume. In order to verify the reproducibility of the test and obtain a ρ value that is the average of several replicates, pycnometer analysis was carried out six times. The ρ of a fiber is a fundamental parameter for the calculation of its aerodynamic diameter (D_{ae}) (Gualtieri et al. 2017; Gualtieri 2018). D_{ae} influences the deposition depth of inhaled particles in the airways (Yeh et al. 1976; Heyder et al. 1986). Particles with $D_{ae} > 5$ μm are deposited in the nasal respiratory tract, whereas particle with $3 \leq D_{ae} \leq 15$ μm are deposited in the lower respiratory tract that extends from the trachea to the lungs (Yeh et al., 1976; Heyder et al., 1986; Gualtieri et al. 2017). Particles with $D_{ae} \approx 2\text{-}3$ and < 0.2 can easily settle in the alveolar space (Gualtieri et al. 2017), which is the main focus of respiratory diseases (French 2009). D_{ae} can be calculated using the equation by Gonda and Abd El Khalik (1985).

Thermogravimetric measurements and evolved gas analysis with mass spectrometry

Thermogravimetric and differential thermal analysis (TG and DTA) measurements were performed with a Seiko SSC 5200 (Chiba, Japan) thermal analyzer coupled with a quadrupole mass spectrometer ESS, GeneSys Quadstar 422 (ESS Ltd. Cheshire, UK) to identify the gases evolved during heating (i.e., mass spectrometry of evolved gas analysis, MS-EGA). Gas sampling by the spectrometer was via an inert, fused silicon capillary system, heated to prevent the condensation of gases. Measurements were performed on air-dried samples under the following experimental conditions, heating rate: 20 °C/min; heating range: 20–1200 °C; TG and DTA data measurement: every 0.5 s; purging gas: ultrapure helium, flow rate: 100 $\mu L \cdot min^{-1}$. MS-EGA were carried out in multiple ion detection (MID) mode measuring the signal of the m/z ratios 17 and 18 for H_2O, 28 and 44 for CO_2, 30 for NO, 34 for H_2S, 46 for NO_2 and 64 for SO_2 (m/z is the dimensionless ratio between the mass number (m) and the charge (z) of an ion); secondary electron multiplier detector at 900 V were employed with 1.0 s of integration time on each measured mass. To avoid differences in relative humidity, samples were isothermally equilibrated at 25 °C for 15 min inside the oven using a 100 $\mu L \cdot min^{-1}$ flow of ultrapure He.

Mössbauer spectroscopy

Room Temperature Mössbauer spectra were collected at the Department of Chemical Science, University of Padua, using a conventional constant acceleration spectrometer mounting a ^{57}Co source, nominal strength 1850 MBq. The hyperfine parameters isomer shift (δ), quadrupole splitting (Δ), half linewidth at half maximum (Γ_+) were expressed in mms^{-1}, while internal magnetic field (B) in Tesla (T) and the relative area (A) in %. The parameters were obtained by least-squares minimization analysis. The absorber was prepared by mixing ~90 mg of gently crushed sample with Vaseline. Due to the low amount of Fe in the absorber (≈1 wt %), the thin absorber thickness is assumed (Long et al. 1983). Concerning the evaluation of the ratio Fe^{2+} over Fe^{3+} in the chrysotile, the recoilless fractions *f* for Fe^{2+} and Fe^{3+} were considered equal. This approximation is acceptable because the error affecting the area evaluation is higher than the one obtained without using the *f* correction (Chukanov et al.

2019). Quantitative analysis was performed using Recoil software, and a reduced χ^2 method was used to evaluate goodness of fit (Lagarec and Rancourt 1998).

Fourier Transform Infra-Red (FTIR) spectroscopy

FTIR analyses were performed on sample powders in the spectral range 500–4000 cm^{-1} using a Bruker Vertex 70 spectrometer (Ettlingen, Germany) equipped with a DTGS detector and a KBr beam splitter. The spectrometer was coupled to a horizontal attenuated total reflectance (ATR) device consisting of a diamond crystal of 2 mm in diameter (Platinum ATR-QL, Bruker Optics, Ettlingen, Germany). The nominal resolution was set at 2 cm^{-1}, and 32 scans were accumulated for both sample and background.

X-ray photoelectron spectroscopy (XPS)

XPS measurements were conducted to determine the Fe^{2+}/Fe^{3+} ratio close to surface layers of the chrysotile fibers. XPS spectra were acquired with a CLAM2 VG Microtech electron hemispherical analyzer operated at 30 eV of pass energy (0.6 eV of energy resolution) at normal emission and a double anode XR3 VG source, delivering Mg Kα photons (1253.6 eV), at 15 kV, 18 mA.

Electron probe micro analysis (EPMA)

Quantitative chemical composition of the sample was obtained using a JEOL 8200 SuperProbe Electron Probe Microanalyzer equipped with a Wavelength-Dispersive X-Ray (WDS) spectrometer and W hairpin type filament. Detectable wavelength is 0.087 to 9.3 nm. Atomic number resolution on BSE (Z): less/equal than 0.1 (CuZ). The following analytical conditions were used: excitation voltage of 15 kV, specimen current of 5 nA, peak-count time of 30 s, background-count time of 10 s. The instrument is also equipped with EDX system characterized by a detectable element range: Na to U, energy resolution: 144 eV and lithium (Li)-doped silicon single-crystal semiconductor detector. Specimen was prepared by embedding an aliquot of the sample in epoxy resin (shaped into a disc with a diameter of 25 mm) and polishing it to achieve a flat, shiny surface. For each spot analysis the following elements

were determined: Si, Ti, Al, Cr, Mn, Mg, Ca, Na, K, Ni, Fe, Pb, Co, V and Cu. The standards utilized were: elemental vanadium for V, elemental chromium for Cr, elemental cobalt for Co, elemental copper for Cu, nickeline for Ni, galena for Pb, omphacite for Na, orthoclase for K, mercuric sulfide for Hg, rhodonite for Mn, forsterite for Mg, fayalite for Fe, ilmenite for Ti, grossular garnet for Al, Si and Ca. Analysis of the individual fibers was not possible because the fibers were invariably aggregated in bundles and clusters (Fig. 1S in Supplementary Materials) and the beam spot size (1 μm) was greater than the average diameter of fibrous particles. The position of each spot analysis was selected using semi-quantitative EDX analysis.

Inductively coupled plasma mass spectrometry (ICP-MS)

ICP-MS was used to determine the concentration of selected (Gualtieri 2018) and potentially toxic elements (i.e., Sb, As, Be, Cd, Co, Cr, Cu, Pb, Mn, Ni, Zn and V). Approximately 50 mg of three different aliquots of sample powder were digested with Suprapur® grade HF and HNO_3 in a Teflon capsule heated at 200 °C. Solutions were analyzed through a quadrupole Thermo X Series-2 ICP-MS spectrometer using the kinetic energy discrimination (KED) approach. Calibration curves were prepared using a Merck (Darmstadt, Germany) ICP multi-element certified standard solution. Yttrium was added both to samples and solutions as internal standard.

Biodurability

The biodurability of asbestos fibers was investigated using *in vitro* methods (Pollastri et al. 2016b; Gualtieri et al. 2018b; Gualtieri et al. 2019b). Pollastri et al. (2016b) performed a comparative study on the biodurability of chrysotile and crocidolite using human mesothelial and alveolar cells. Results of this study showed that after 96 h of contact with cell cultures, chrysotile fibers were partially dissolved and amorphized, whereas, after the same exposure time, crocidolite fibers showed very minor signs of amorphization (Pollastri et al. 2016b). *In vitro* acellular studies conducted by Gualtieri et al. (2018b) show that chrysotile fibers in contact with simulated lung fluids (SLF) undergo decomposition of the

369 octahedral layer with leaching of Mg and amorphization. In the present study the determination of
370 biodurability of Yasniy chrysotile was evaluated by *in vitro* acellular dissolutions tests in batch reactors
371 at 37 °C (Gualtieri et al. 2018b). More specifically, our leaching tests were conducted using 25 mg of
372 sample and 250 ml of artificial lysosomal fluid (ALF) solution at pH=4 (Marques et al. 2011; Gualtieri
373 et al. 2018b). ALF was used to reproduce the macrophage intracellular phagolysosome chemical
374 environment mimicking the phagocytosis process inside the alveolar space. The degree of dissolution
375 was determined by measuring the change of the sample mass after different times: 24h, 48h, 1 week, 2
376 weeks, 1 month, 2 months and 3 months. The mass of the sample dissolved was used to determine the
377 apparent dissolution rate R ($mol \cdot m^{-2} s^{-1}$):

$$R = \frac{k}{SSA \cdot m}$$

378 with SSA determined using the BET-method (see section *2.6*), m = initial mass of the sample (g) and k
379 = apparent dissolution rate constant. In addition, assuming that the whole sample consisted of fibers,
380 the estimated lifetime t of a fiber was determined using the equation (originally applied to chrysotile by
381 Hume and Rimstidt 1992):

$$t = \frac{3w}{4VR}$$

382 where w = fiber width (m) and V = molar volume ($m^3 \cdot mol^{-1}$). Detailed description of dissolution
383 methods and data analyses are reported in Gualtieri et al. (2018b).

384

385 **DETERMINATION OF THE FPTI OF YASNIY CHRYSOTILE**

386 To calculate the FPTI of a mineral fiber, we used a model incorporating morphometric, chemical,
387 biodurability related, and surface parameters of mineral fibers that affect their toxicity and
388 pathogenicity upon inhalation (Gualtieri 2018; Mossman and Gualtieri 2020). Although a detailed
389 description of the parameters is reported in Gualtieri (2018), a short summary is reported below.

The length and width of mineral fibers are key factors in toxicity, inflammation and pathogenicity of mineral fibers (Stanton et al. 1981; Berman and Crump, 2008a; 2008b; Donaldson et al. 2010; Mossman and Gualtieri 2020) while the surface curvature of the fibers affects the binding process of proteins and influences cell adhesion (Churg, 1993; Deng, 2012). The crystal habit of a fiber influences its depositional pathway in the respiratory tract (Gualtieri et al. 2017) while the density determines its aerodynamic diameter and therefore it affects the deposition depth of inhaled fiber in the airways (Gualtieri 2018). The hydrophobic character of a fiber rules the interaction with biopolymers (i.e., proteins) and phagocytic cells (Gualtieri et al. 2017; Gualtieri 2018) while the surface area affects the dissolution kinetics and biodurability, the resistance to chemical/biochemical alteration (Donaldson et al. 2010; Gualtieri et al. 2018b).

Iron (mainly Fe^{+2}) at the surface of mineral fibers promotes the formation of the reactive oxygen species (ROS) and reactive nitrogen species (RNS), with cyto- and genotoxic effects (Gualtieri et al. 2019c). To be active, iron sites must occur at the surface of the fiber in contact with the cell or cell medium. Reactivity of iron is also related to its nuclearity (Gualtieri 2018). Metals other than iron prompt inflammation activity *in vivo* (Gualtieri et al. 2019b).

Dissolution rate is a key parameter, because if a fiber rapidly dissolves in lung environment, it is assumed to have a low biodurability and in principle is less toxic than a fiber with high biodurability (Gualtieri et al. 2017). Numerous studies indicated that a mineral fiber might be toxic if it is sufficiently durable to remain unaltered within the lung tissue and induce a chronic inflammatory (Gualtieri et al. 2017; Carbone et al. 2019). Accordingly, the high biodurability of the amphibole asbestos accounts for their high toxicity. While the low biodurability of chrysotile explains its relative low toxicity (Bernstein et al. 2014; 2015; Bernstein and Pavlisko 2017).

The rate of dissolution of iron, silica and metals controls the release into the extracellular space of substances that may generate the reactive oxygen species (ROS) (Gualtieri et al. 2019b).

The electric charges surrounding the fibers, measured as zeta potential, may correlate with a number of phenomena responsible for adverse effects (Pollastri et al. 2014). Zeta potential also influences the agglomeration of the fibers (Pollastri et al. 2014).

Table 1 summarizes the parameters of the model used for the calculation of the FPTI of Yasniy chrysotile. For each parameter, a score is assigned depending on its measured value and its supposed capability in inducing adverse effects (Table 1). Because the parameters of the model can be correlated with each other, a hierarchical scheme considering the cross-correlations is applied (Gualtieri 2018; Mossman and Gualtieri 2020). Weighing scheme is associated with each parameter of the model according to its step/hierarchy H where $w_1 = 1/H$ with H = 1, 2 or 3. A weight defined as $w_2 = 1/U$ is also applied to each parameter of the model. This accounts for the uncertainty in the determination of a specific parameter (n, m) and is defined by the penalty parameter U (1 = low to null uncertainty, 2 = some degree of uncertainty, 3 = high uncertainty). Having defined the weighing scheme of the parameters, the $FPTI_i$ is calculated according to the equation (Gualtieri 2018):

$$FPTI_i = \sum_{i=1}^{n} w_1 . w_2 . T_i$$

with T_i = class value of the parameter i of the model; $w_1 = 1/H$ weight of the parameter according to its hierarchy H; $w_2 = 1/U$ weight of the parameter according to the uncertainty U of its determination. Table 1 reports the parameters of the model used for the calculation of the FPTI, their classification and relative normalized scores $FPTI_i$.

RESULTS

The magnified XRPD pattern (7-80 °2θ) of the sample is shown in Figure 2. The qualitative mineralogical analysis showed that the raw material from Yasniy mine mainly contains clinochrysotile (Ctl) with minor ortho-chrysotile (Ctl) and lizardite 1T (Liz, minor). Minor amounts of magnetite

436 (Mag) and traces of hydromagnesite (HM) were also detected. Only the major peak of calcite was
437 identified.

438 A gallery of FEG-SEM and STEM images of the Yasniy chrysotile is reported in Figure 3. Yasniy
439 chrysotile is characterized by bundles of long and very thin fibrils (Figs. 3a and 3b). Bundles are
440 mostly composed of parallel long and flexible fibers that exhibit "split-ends" (Figs. 3a and 3b). Bundle
441 lengths range between 20 μm and 1 mm (Fig. 3a). The statistics of a representative number of
442 individual fibers are reported in Table 2. The data display a wide range of lengths, with values ranging
443 from 1.36 to 188 μm (average 27.2 μm), but the longer fibers predominate in the population. More than
444 75% of the fibers are longer than 15 μm. The overall widths of the fibers range between 0.05 and 1.65
445 μm, and 50% of the fibers show a width of less than 0.59 μm. Representative EDX spectra are attached
446 as Supplementary Material (Fig. 2S). EDX microanalyses of some fiber bundles showed the presence
447 of two main chemical compositions indicative of chrysotile and magnetite (Fig. 2S in Supplementary
448 Materials). As shown in STEM images, particles of magnetite are interspersed within the chrysotile
449 bundles (Figs. 3c and d).

450 Figure 4 shows some selected images of the chrysotile fibers observed with PCOM. The measured
451 optical parameters of the Yasniy chrysotile are reported in Table 3. PCOM analysis with the
452 appropriate refractive liquids (n = 1.550) shows that Yasniy chrysotile fibers turn purple or blue in
453 color, with distinctive dispersion colors associated with chrysotile (Tylee et al. 1996).

454 Specific surface area (SSA) of the Yasniy chrysotile is 18.4(5) m^2g^{-1}. Table 4 reports the SSA of the
455 investigated sample and other mineral fibers (Gualtieri et al. 2018b). SSA of the Yasniy sample is two
456 times smaller than the SSA of the UICC chrysotile standard and Balangero sample. Valmalenco
457 chrysotile has SSA three time higher than Yasniy sample. Although SSA of the Yasniy chrysotile is
458 comparable with that of crocidolite asbestos, its value is higher than the SSA of most amphibole
459 asbestos (Table 4). SSA is a parameter that affects the biodurability and biopersistence of mineral

460 fibers (Gualtieri et al. 2018b) In particular, the SSA directly influences the dissolution rate of a fiber
461 and is included as a factor in the equation used to determine the apparent dissolution rate (R) (Table 4).
462 A larger surface area determines a higher reactivity of the mineral fibers in solution. In acidic
463 environment (as the one found in lung tissue) particles with large surface area (e.g. Valmalenco
464 chrysotile fibers) are more reactive than those with low SSA (Gualtieri et al. 2018b).

465 Results of the zeta potential analyses as a function of pH are reported in Figure 5. Measurements
466 carried out in double-distilled water (Fig. 5a) match with the literature data, showing that chrysotile has
467 positive values of the zeta potential in this dispersion media (Pollastri et al. 2014). The zeta potential
468 values in double-distilled water match those reported for UICC chrysotile in Pollastri et al. (2014),
469 although the value of Yasniy chrysotile is more positive at alkaline pH (Fig. 5a). In the ALF solution,
470 the zeta potential of Yasniy chrysotile turns from positive to negative. In contact with the ALF solution,
471 the Yasniy chrysotile shows zeta potential values very similar to those found for the UICC chrysotile
472 (Fig. 5b). In the pH range between 2 and 10, the zeta potential of the sample varies from 37 to 14 using
473 double-distilled water as a dispersion media, while from 15 to -23 using ALF solution. Overall, when
474 the pH of the suspension increases, the zeta potential decreases in double-distilled water and becomes
475 more negative in ALF solution (Fig. 5).

476 The density of Yasniy chrysotile is 2.578 (0.002) $g.cm^{-3}$, which is consistent with those reported in
477 the literature, i.e., 2.5-2.6 $g.cm^{-3}$ (Thomassin et al. 1997; Jolicoeur and Duchesne 1981; Jaurand et al.
478 1983; Sprynskyy et al. 2011).

479 Results of the combined TG-DTA analysis of the sample are reported in Figure 6a. The first
480 derivative of the TG curve (DTG) shows five main thermal events, well paralleled by MS-EGA curves
481 (Fig. 6b), with maximum reaction rates at 75, 223, 384, 656 and 662 °C. The reaction at 75 °C is due to
482 the loss of adsorbed water (weight loss 0.28 wt% in the thermal range 25-135°C). The reactions at 223
483 and 384 °C may be, respectively, related to dehydroxylation (Frost and Erickson 2004; Khorami et al.

1984) and decarbonation (Vágvölgyi et al. 2008) of hydrated carbonates as, for example, hydrotalcite-like phase (though not detected through XRPD). The shoulders on the DTG curve at 535 and 592 °C are also deemed to be generated by a second release of CO_2, ascribed to carbonates present as minor impurities (Gallagher and Warne 1981) and undetected by XRPD. The two major thermal events at 656 and 662 °C, partially overlapped, are due to the chrysotile dehydroxylation (Kohyama et al. 1996; Viti 2010; Bloise et al. 2016a), as also highlighted by the wide endothermic bump on the DTA curve (Fig. 6a). These two endothermic events include also minor contributions due to the decarbonation of calcite (Kissinger 1957; Villieras et al. 1994; Viti 2010) as indicated by the simultaneous release of CO_2 (Fig. 6b). The product of the dehydroxylation of chrysotile (recrystallized as forsterite) caused a sharp exothermic peak at 830 °C on the DTA curve (Cattaneo et al. 2003; Bloise et al. 2009; Bloise et al. 2017). The release of CO_2 below 400 °C, more evident in Figure 6b, is also due to the thermal decomposition of organic impurities as proved by the simultaneous release of NO (Rodrigues et al. 2005). Nevertheless, to verify this hypothesis, 20 mg of the sample was treated with 20 ml of an organic solvent (i.e., ethyl acetate) for 1 h and after being washed with Millipore water, it was air-dried and analyzed under the same experimental conditions. The thermo-analytical curves of the ethyl acetate treated sample (Figs. 6c and 6d) basically parallel those of the untreated one, except for two main changes. First, there is an evident decrease of the reaction with a maximum at 399 °C in the DTG curve (Fig. 6c) and the disappearance of the signal is related to NO release (Fig. 6d). Second, there is a small gain of adsorbed water which leads to a slight increase in the overall weight loss (Fig. 6c). The complete absence of signals relating to m/z = 34 (H_2S) and 64 (SO_2) indicates that sulfurated compounds are below the limit of detection. The Mössbauer spectrum of the sample is reported in the Supplementary Materials (Fig. 3S). The spectrum shows the presence of magnetically splitting components together with a complex paramagnetic absorption. The best fitting was obtained by using two sextets and two doublets, whose hyperfine parameters are reported in Table 5. The hyperfine

parameters of the two sextets are consistent with those of magnetite. The deviation of the site occupancy ratio from the theoretical value (1:1.9) is indicative of a partial oxidation of the magnetite particles (Chukanov et al. 2019). Concerning the paramagnetic absorption, the two doublets are representative for both Fe^{2+} and Fe^{3+} in octahedral sites, in concert with the literature data (Vandenberghe et al. 2005; Ristić et al. 2011). The Fe^{2+}/Fe^{3+} ratio, calculated considering only the paramagnetic component, is 0.61. It should be remarked that the ferric site shows a value of line width Γ_+ considerably enlarged in comparison with that of the ferrous site. The broadening can be ascribed to the superposition of different Fe^{3+} sites, as suggested by Ristić et al. (2011). No reliable results were obtained attempting to resolve the ferric doublet. For this reason, the presence of a tiny amount of Fe^{3+} in tetrahedral sites, as consequence of the Si^{4+} substitution, cannot be excluded a priori.

The FTIR spectrum of Yasniy sample is nearly identical to that acquired for the UICC standard chrysotile (Fig. 4S, Supplementary Materials). The spectrum shows the typical bands displayed by serpentine minerals (Hofmeister and Bowey 2006; Rivero Crespo et al. 2019). The intense peaks at 950, 1020 and 1074 cm^{-1} are related to the Si–O bond (Hofmeister and Bowey 2006). The two peaks at 1420 and 1480 cm^{-1} and the strong absorption bands in the range 3800–3500 cm^{-1} can be assigned to the MO–H (M = Fe^{2+} or Mg^{2+}) stretching vibrations modes (Della Ventura 2017; Rivero Crespo et al. 2019).

The XPS spectrum reported in the Supplementary Materials (Fig. 5S), shows the Fe 2p energy region after removal of the X-ray satellite lines from photoelectron spectra excited with Mg *K*α radiation. The spectrum has been decomposed into Voigt doublets, taking onto account the spin-orbit splitting of Fe $2p_{3/2}$ and $2p_{1/2}$ components, over a Shirley-type background. The spectrum presents characteristic Fe^{2+} and Fe^{3+} main components, accompanied by related satellites (Brundle et al. 1977; McIntyre and Zetaruk 1977; Grosvenor et al. 2004). The branching ratio between Fe^{2+}/ Fe^{3+} $2p_{3/2}$ components is 0.86.

This is the peer-reviewed, final accepted version for American Mineralogist, published by the Mineralogical Society of America.
The published version is subject to change. Cite as Authors (Year) Title. American Mineralogist, in press.
DOI: https://doi.org/10.2138/am-2021-7710. http://www.minsocam.org/

The results of the EPMA analyses expressed in weight percent with standard deviations are reported in the Supplementary Material (Table 1S). The chemical formula of Yasniy chrysotile, as determined from 26 EPMA spot analyses is:

$$(Mg_{2.870}Fe^{2+}{}_{0.027}Fe^{3+}{}_{0.045}Al_{0.034}Cr_{0.005}Ni_{0.006})_{2.986}(OH)_4Si_{1.982}O_5$$

The Fe^{2+}/Fe^{3+} ratio is from the Mössbauer analysis. The chemical composition of the investigated chrysotile is comparable to those obtained for the chrysotile samples previously studied by Pollastri et al. (2016a), (Table 1S, Supplementary Material).

Table 6 reports the mean values of the content of metals and potential toxic elements measured by ICP-MS. The concentrations are very high compared with the values found in human lungs (Vanoeteren et al. 1986). Some elements considered as ecological and health risks (As, Cr, Co, Cu, Ni, and Pb) are present in concentrations exceeding recommended limits (Tóth et al. 2016).

The measured value of SSA was used to calculate the kinetic parameters of the *in vitro* acellular dissolution (with ALF solution) of Yasniy chrysotile (Table 1 and Table 4). The dissolution rate of the Yasniy chrysotile (see the apparent rate constant (k) and the apparent dissolution rate (R) in Table 4) is slightly faster that those estimated for other chrysotile samples (Gualtieri et al., 2018b; Gualtieri et al., 2019c).

DISCUSSION

Characteristics of Yasniy chrysotile

In this study, a representative sample of Russian commercial chrysotile obtained from the Yasniy mine, Orenburg region was fully characterized. Qualitative phase analysis from XRPD data confirmed that the sample is mainly composed of chrysotile with minor impurities of lizardite, magnetite, hydromagnesite and possibly calcite. Impurities of organic matter were detected by TG-DTA analyses. The nature of the mineral fiber that characterized the sample was also confirmed by the EPMA, EDX,

555 PCOM and FTIR investigations. The sample from Yasniy mine consists of bundles of very long and
556 thin fibers of chrysotile, most of them showing a high degree of flexibility. Fibers display a curled
557 habit, marked curvature, length > 20 μm and aspect ratio > 3:1. Applying the equation of Gonda and
558 Abd El Khalik (1985) to a typical Yasniy chrysotile fiber with density $\rho = 2.58$ g·cm^{-3} and d = 0.59 μm,
559 the obtained D_{ae} is 1.97 μm. Accordingly, it can be assumed that the chrysotile fibers of the studied
560 sample can easily penetrate through the respiratory tract and settle in the alveolar space (Gualtieri et al.,
561 2017).

562 Although the SSA of chrysotile generally spans from 42 to 68 m^2g^{-1} (Gualtieri et al. 2018b), the
563 Yasniy sample possesses an SSA < 20 m^2g^{-1}. It is important to note that the SSA of a mineral fiber can
564 vary depending on the grain size of the sample (Gualtieri et al. 2017). As shown by the SEM images,
565 Yasniy chrysotile is a coarse material characterized by fibers aggregate in large bundles (Fig. 3a) with a
566 small overall SSA.

567 Similar to chrysotile samples from other locations, the Yasniy sample in contact with the organic
568 solution at pH 4.5 and 7 has negative values of zeta potential, i.e., -8.12 and -20 mV, respectively.
569 Negative zeta potential may prompt the formation of hydroxyl radicals, affects apoptosis and favors the
570 binding of collagen and redox-activated Fe-rich proteins (Pollastri et al. 2014). In addition, at such low
571 zeta potential values, particle agglomeration is favored (Pollastri et al. 2014). Agglomeration of long
572 chrysotile fibers induce high biological response in terms of frustrated phagocytosis (Gualtieri 2018).

573 The total Fe content and Fe^{2+}/Fe^{3+} ratio are important parameters to be considered for the asbestos-
574 induced patho-biological activity (Gualtieri 2018; Gualtieri et al. 2019b). In the crystal structure of
575 chrysotile both Fe^{2+} and Fe^{3+} ions can replace Mg in the octahedral sheet (Pollastri et al., 2015). The
576 analyzed chrysotile fibers have a relatively low ferrous (FeO wt% < 1) and total iron (Fe_2O_3+FeO wt%
577 > 1) content (Table 1S, Supplementary Material).

This is the peer-reviewed, final accepted version for American Mineralogist, published by the Mineralogical Society of America.
The published version is subject to change. Cite as Authors (Year) Title. American Mineralogist, in press.
DOI: https://doi.org/10.2138/am-2021-7710. http://www.minsocam.org/

Results obtained by using XPS match with Mössbauer data: the latter shows a high Fe^{3+} content in the bulk material while the former reveal the presence of a major fraction of Fe^{3+} with respect to Fe^{2+} at the surface of the chrysotile fibers.

Among the considered chrysotile species, the dissolution rate of the Yasniy sample is faster than that of the other chrysotiles (Table 4) and the difference in the dissolution time of chrysotile asbestos with respect to amphibole asbestos is striking (Table 4). After about 130 days, the chrysotile samples are completely dissolved. On the other hand, asbestos amphiboles totally dissolve only after 50 years (Table 4).

Toxicity/pathogenicity potential of Yasniy chrysotile

Figure 7 shows a plot of the FPTI index of Yasniy chrysotile (FPTI = 2.40) and other mineral fiber species. Indicatively, all the amphibole asbestos (amosite UICC standard, crocidolite UICC standard and fibrous tremolite from Val d'Ala, Italy) display FPTI values > 2.50, whereas all chrysotile asbestos samples have values in the range 2.20–2.45. As already observed by Gualtieri (2018), the differences in terms of FPTI index of chrysotile compared to amphiboles asbestos are related primary to the different biodurability of these mineral fiber species. Nevertheless, the FPTI indices of Yasniy sample and the other chrysotile asbestos are markedly greater than those of the fibrous sepiolite from Vallecas (Spain) and commercial wollastonite NYAD G (USA) that have been considered as negative standards (i.e., mineral fibers that according to the literature data do not display toxicity/pathogenicity effects). Accordingly, the chrysotile sample from the Yasniy mine can be considered a potential health hazard, just like other chrysotile samples, and inhalation of this mineral fiber may lead the initiation or onset of health diseases typically associated with exposure to asbestos (IARC 2012). Table 1 reports the FPTI index calculated for the Yasniy chrysotile sample and the normalized score $FPTI_i$ associated with each parameter of the FPTI model (Gualtieri 2018). The same data concerning UICC standard chrysotile and chrysotile samples from Balangero and Valmalenco, have been reported for comparison (Table 1). The

602 FPTI indices assigned to Yasniy and Balangero specimens are very similar (2.40 for Yasniy chrysotile
603 and 2.35 for Balangero chrysotile). Although both chrysotiles have relatively low biodurability, they
604 possess physical/chemical and morphological parameters which may induce biochemical mechanisms
605 responsible for adverse effects *in vivo* (Gualtieri 2018). For instance, Yasniy and Balangero chrysotile
606 display an asbestiform habit (i.e., these minerals grow in a fibrous aggregate of curled, flexible,
607 cylindrical, long, and thin crystals that readily separate) and their fibers have an aerodynamic diameter
608 which makes them breathable. Both chrysotile samples have structural iron which can cause H_2O_2-
609 mediated release of free cytotoxic and genotoxic radicals responsible for adverse effects (Gualtieri et
610 al. 2019b). In the octahedral sites of these mineral fibers, there are potentially toxic metals, which can
611 be released during fiber dissolution (Bloise et al. 2016b). These metals may contribute to promote
612 adverse effects *in vivo* of chrysotile fibers (Gualtieri et al. 2019c). The zeta potential of chrysotile fibers
613 under intracellular conditions (i.e., at pH 4.5) displays values in the range −10 to −20 mV. Such zeta
614 potential values, may affect several molecular and cellular biomechanics such as cross-talk and
615 apoptosis mechanisms, fiber encapsulation by collagen and redox-activated iron-rich proteins, and the
616 ROS/RNS generation (Pollastri et al. 2014). The coarse size of the fiber aggregates possessed by the
617 Yasniy chrysotile determines a relatively low specific surface area compared to the Balangero
618 chrysotile. At the same time, the Balangero chrysotile has an average fiber width greater than that of
619 the Yasniy chrysotile. These differences in morphological parameters (1,2) and (1,7), are the reason for
620 the slightly higher FPTI value of the Yasniy chrysotile than the Balangero sample (Table 1). It is also
621 important to note that the chrysotile extracted from the Yasniy mine may have been pre-processed
622 before being packaged. Therefore, the processes that the chrysotile underwent may have influenced its
623 morphological characteristics. A closer look at the plot (Fig. 7) reveals that the FPTI of Yasniy
624 chrysotile is significantly higher than that UICC standard chrysotile (FPTI = 2.22) and the samples
625 from Valmalenco (FPTI = 2.25). Regarding the UICC chrysotile, the main difference compared to

626 other samples concerns the content of trace elements, i.e., the parameters (1,11) and (1,15). Namely,
627 the UICC chrysotile has a significantly lower metal content than the other chrysotiles. Considering the
628 data reported by Bloise et al. (2016b) and the results of this study (Table 6), the standard UICC
629 chrysotile contains 1704 $mg.kg^{-1}$ of V+Cr+Mn+Ni, while Yasniy, Balangero and Valmalenco samples
630 contain 13473, 2064 and 2044 $mg.kg^{-1}$ of V+Cr+Mn+Ni, respectively. These differences in terms of
631 trace element content can be attributed to the different genetic environments and conditions. Chrysotile
632 is a serpentinization product of ultramafic rocks (Viti 2010; Zucchetti et al. 1988) and originates from
633 hydrolysis and transformation of primary ferromagnesian minerals, such as olivine and orthopyroxene
634 in peridotite (Holm et al. 2015). These minerals are progressively replaced by variable amounts of
635 serpentine minerals (mainly chrysotile and lizardite), Ni-Fe alloys, talc, chlorite, tremolite/actinolite
636 and brucite, depending on pressure and temperature conditions (Holm et al. 2015). Consequently, the
637 crystalline chemistry of chrysotile reflects the chemical composition of the replaced minerals and the
638 host rock. The UICC Chrysotile Standard consists of a mixture of fibers from eight mines in Quebec,
639 Canada (i.e., Bells, Carey, Cassair, Flintkote, Johns-Manville, Lake, Normandie and National). The
640 fibers are mixed in proportion to the annual production of these asbestos mines (Timbrell et al. 1968;
641 Gunter et al. 2007; Pollastri et al. 2016a). The host rock of Quebec chrysotile deposits is for mostly
642 harzburgite (Cogulu and Laurent 1984). Instead, the main host rock types within the ophiolite massifs
643 of Orenburg Region, where the Yasniy mine is located, are harzburgite with subordinate dunite
644 (Gannoun et al. 2003). The Balangero serpentinite deposit derived from a metamorphic spinel-
645 plagioclase lherzolite-harzburgite (Zucchetti et al. 1988). Valmalenco chrysotile occurs in serpentinized
646 peridotites, and subordinately spinel-lherzolites, garnet clinopyroxenites, spinel-websterites, dunites
647 and harzburgites (Cavallo and Petriglieri 2020; Münterer and Hermann 1996). As far as Valmalenco
648 chrysotile is concerned, the main difference compared to other chrysotile samples lies in the average
649 length of the fibers. Specifically, Valmalenco chrysotile shows shorter fibers than other chrysotile

650 samples (Table 1). Overall, the differences in the fiber geometry (parameter 1,1 and 1,2) between
651 Valmalenco/Balangero chrysotiles and other samples may be consequence of the serpentine
652 polymorphism. In this regard, recent research has revealed a significant presence of lizardite and
653 antigorite in the Balangero/Valmalenco chrysotiles (Pollastri et al. 2016a). On the contrary, Yasniy
654 sample and UICC standard are mainly composed of chrysotile (Pollastri et al. 2016a). Furthermore, it
655 should be pointed out that the preparation of UICC standards involves a grinding process before mixing
656 (Timbrell et al. 1968), which may have affected the morphology of the UICC chrysotile.

657 The Yasniy chrysotile differs from the other samples, not only for the smaller SSA, but also for a
658 lower FeO wt% content (Table 1). As mentioned above regarding the differences in terms of metal
659 concentration, the iron content of the chrysotile samples is also linked to the crystallization conditions
660 and the serpentinization process. In particular, the Fe^{+2}/Fe^{+3} ratio is closely related to the
661 reductive/oxidative conditions during the mineral genesis (Ristić et al. 2011). The comparatively high
662 Fe^{+2}/Fe^{+3} ratios, in the case of Balangero ($Fe^{+2}/Fe^{+3} = 1.66$) and Valmalenco ($Fe^{+2}/Fe^{+3} = 1.20$) samples
663 (Pollastri et al. 2016a), may be due to the formation of chrysotile under poorly oxidative (or reductive)
664 conditions. On the other hand, a low content of Fe^{+2} in Yasniy ($Fe^{+2}/Fe^{+3} = 0.61$) and UICC standard
665 ($Fe^{+2}/Fe^{+3} = 0.50$) samples shows that these minerals have been formed under highly oxidative
666 conditions.

667 In agreement with previous studies (Gualtieri et al. 2018b; 2019c) the results of *in vitro* acellular
668 dissolutions tests shown in this work confirm that chrysotile is less biodurable than amphibole asbestos.
669 To a first approximation, the outcome of the biodurability tests supports the "amphibole hypothesis"
670 for which a lower biodurability of chrysotile is reflected in a lower toxicity potential of this mineral
671 fiber with respect to amphibole asbestos. Nevertheless, in accordance with the model proposed by
672 Gualtieri et al. (2019c), the low durability of chrysotile can induce an acute toxicity effect similar to
673 that associated with nanoparticles and commonly called "Trojan horse effect"(Studer et al. 2010).

Yasniy chrysotile, like nanoparticles, undergoes fast dissolution during phagocytosis and becomes a carrier of high levels of toxic metals (e.g., Fe, Co, Cu, Cr and Ni). These metals when released into the cytoplasmic space catalyze oxidation-reduction reactions leading to the formation of ROS/RNS that can induce protein oxidation, lipid peroxidation and DNA damage (Gualtieri et al. 2019b; 2019c). Hence, 'Trojan horse effect' must be considered in the definition of the potential toxicity/pathogenicity of Yasniy chrysotile.

To summarize, a biodurable fiber like amphibole asbestos is responsible for long term effects *in vivo* due to chronic frustrated phagocytosis and is reasonably assumed to be potent in inducing malignant mesothelioma, the characteristic asbestos induced lung disease with a long latency period. Biodurable amphibole asbestos is also responsible for short term toxic effects *in vivo* due to the production of ROS and other reactive species by iron present at the fiber surface, by frustrated phagocytosis but not by release of metals in the short term. A non-biodurable fiber like chrysotile appears less prone to induce long term chronic effects *in vivo* and for this reason is assumed to be less potent in inducing malignant mesothelioma. On the other hand, silica relicts produced by the dissolution of chrysotile may be eventually responsible for mid/long term chronic effects *in vivo* due to reiterated frustrated phagocytosis and eventually production of ROS at the reacting surface (Gualtieri et al. 2019a). Chrysotile dissolution is undoubtedly responsible for short term toxic effects *in vivo* because, in addition to the effects displayed by the biodurable fibers described above, fast release of metals and subsequent production of ROS and other reactive species is promoted.

IMPLICATIONS

In this study, a representative commercial chrysotile sample from the Orenburg ore mine near the city of Yasniy (Russia), was fully characterized using a suite of experimental techniques, and its toxicity/pathogenicity potential was assessed using the FPTI model. The FPTI of the Russian chrysotile

698 is lower than that of the amphibole asbestos, but higher than the threshold limit set for "safe" mineral
699 fibers. Furthermore, the acquired analytical data showed that the Yasniy chrysotile shares several
700 chemical-physical characters with other chrysotiles (UICC standard, Balangero and Valmalenco, Italy)
701 known to prompt adverse effects *in vivo*.

702 Although, studies concerning Russian chrysotile are few, there is some evidence that Ural chrysotile
703 deposits may contain tremolite (Tossavainen, et al. 2000; Schüz, et al. 2013). In contrast, the Orenburg
704 chrysotile studied in this work does not contain amphibole asbestos. This peculiarity makes Yasniy
705 chrysotile suitable for future *in vitro* and *in vivo* tests, which can provide further experimental
706 confirmation of the outcome of our work. At the same time, the Yasniy town and the Orenburg region
707 are excellent candidates for epidemiological studies concerning the chrysotile-related diseases.

708 Finally, we believe that the approaches used in this study, for quantitatively assessing the
709 toxicity/pathogenicity of the Russian chrysotile, can be applied to commercial chrysotile samples in
710 other places.

711

712 **Acknowledgements**

713 This research was conducted under the project "*Fibres A Multidisciplinary Mineralogical, Crystal-*
714 *Chemical and Biological Project to Amend The Paradigm of Toxicity and Cancerogenicity of Mineral*
715 *Fibres*" (PRIN: PROGETTI DI RICERCA DI RILEVANTE INTERESSE NAZIONALE – Bando
716 2017 - Prot. 20173X8WA4). The study was further supported in part by the project "CCIAARE -
717 Attuazione di un progetto di accompagnamento delle imprese nell'ambito del progetto PID impresa
718 4.0" financed by the Camera di Commercio di Reggio Emilia (Italy). Authors are grateful to Evgeny
719 Kuznetsov (Sibelco Rus LLC) and Enrico Sopini (Sibelco Italia S.p.A.) for providing the chrysotile
720 sample. Authors warmly thank all the collaborators who contributed to the experimental part of the
721 work: Umberto Tessari, Gianluca Malavasi, Mauro Zapparoli, Daniela Manzini and Francesca Marino.

We also thank Messori Roberto and the staff of the ARPAe Reggio Emilia for their help with the PCOM analyses.

Declaration of Competing Interest

The authors declare that there are no conflicts of interest.

References

Baietto, O., and Marini, P. (2018) Naturally occurring asbestos: Validation of PCOM quantitative determination. Resources Policy, 59, 44-49.

Ballirano, P., Bloise, A., Gualtieri, A.F., Lezzerini, M., Pacella, A., Perchiazzi, N., Dogan, M., and Dogan, A.U. (2017) Crystal habit of mineral fibres. In A.F. Gualtieri, Ed., Mineral Fibres: Crystal Chemistry, Chemical-Physical Properties, Biological Interaction and Toxicity, 18, p. 11-53. EMU Notes in Mineralogy, European Mineralogical Union, London.

Berman, D.W., and Crump, K.S. (2008a). Update of potency factors for asbestos-related lung cancer and mesothelioma. Critical reviews in toxicology, 38, 1-47.

Berman, D.W., and Crump, K.S. (2008b). A meta-analysis of asbestos-related cancer risk that addresses fiber size and mineral type. Critical reviews in toxicology, 38, 49-73.

Bernstein, D.M., Chevalier, J., and Smith, P. (2005) Comparison of Calidria chrysotile asbestos to pure tremolite: final results of the inhalation biopersistence and histopathology examination following short-term exposure. Inhalation Toxicology, 17, 427-449.

Bernstein, D., Dunnigan, J., Hesterberg, T., Brown, R., Velasco, J.A.L., Barrera, R., Hoskins J., and Gibbs, A. (2013) Health risk of chrysotile revisited. Critical Reviews in Toxicology, 43, 154-183.

Bernstein, D.M., Rogers, R., Sepulveda, R., Kunzendorf, P., Bellmann, B., Ernst, H., and Phillips, J.I. (2014) Evaluation of the deposition, translocation and pathological response of brake dust with and without added chrysotile in comparison to crocidolite asbestos following short-term inhalation: Interim results. Toxicology and Applied Pharmacology, 276, 28-46.

753 Bernstein, D.M., Rogers, R.A., Sepulveda, R., Kunzendorf, P., Bellmann, B., Ernst, H., Creutzenberg,
754 O., and Phillips, J.I. (2015) Evaluation of the fate and pathological response in the lung and pleura
755 of brake dust alone and in combination with added chrysotile compared to crocidolite asbestos
756 following short-term inhalation exposure. Toxicology and Applied Pharmacology, 283, 20-34.
757 Bernstein, D.M., and Pavlisko, E.N. (2017) Differential pathological response and pleural transport of
758 mineral fibres. In A.F. Gualtieri, Ed., Mineral Fibres: Crystal Chemistry, Chemical-Physical
759 Properties, Biological Interaction and Toxicity, 18, p. 417-434. EMU Notes in Mineralogy,
760 European Mineralogical Union, London.
761 Bloise, A., Belluso, E., Barrese, E., Miriello, D., and Apollaro, C. (2009) Synthesis of Fe-doped
762 chrysotile and characterization of the resulting chrysotile fibers. Crystal Research and Technology,
763 44, 590-596.
764 Bloise, A., Catalano, M., Barrese, E., Gualtieri, A.F., Gandolfi, N.B., Capella, S., and Belluso, E.
765 (2016a) TG/DSC study of the thermal behaviour of hazardous mineral fibres. Journal of Thermal
766 Analysis and Calorimetry, 123, 2225-2239.
767 Bloise, A., Barca, D., Gualtieri, A.F., Pollastri, S., and Belluso, E. (2016b) Trace elements in hazardous
768 mineral fibres. Environmental Pollution, 216, 314-323.
769 Bloise, A., Kusiorowski, R., Lassinantti Gualtieri, M., and Gualtieri, A.F. (2017) Thermal behaviour of
770 mineral fibres. In A.F. Gualtieri, Ed., Mineral Fibres: Crystal Chemistry, Chemical-Physical
771 Properties, Biological Interaction and Toxicity, 18, p. 215-252. EMU Notes in Mineralogy,
772 European Mineralogical Union, London.
773 Bruker AXS (2019) DIFFRAC.EVA V5.1. [Online] Available: https://www.bruker.com/products/x-
774 ray-diffraction-and-elemental-analysis/x-ray-diffraction/xrd-software/eva.html [accessed 2020
775 March 14]. Bruker AXS, Karlsruhe, Germany.
776 Brunauer S., Emmet, P.H., and Teller, E. (1938) Adsorption of gases in multimolecular layers. Journal
777 of the American Chemical Society, 60, 309-319.
778 Brundle, C.R., Chuang, T.J., and Wandelt, K. (1977) Core and valence level photoemission studies of
779 iron oxide surfaces and the oxidation of iron. Surface Science, 68, 459-468.
780 Burkhanova, R.A., Kovtunov, I.A., and Azarov, V.N. (2019) Investigation of the Parameters of
781 Discarded Dust in the Manufacture of Products from Chrysotile Asbestos and Cement. IOP
782 Conference Series: Earth and Environmental Science, 272, 022150.

783 Cametti, G., Pacella, A., Mura, F., Rossi, M., and Ballirano, P. (2013) New morphological, chemical,
784 and structural data of woolly erionite-Na from Durkee, Oregon, U.S.A. American Mineralogist, 98,
785 2155-2163.
786 Camus, M. (2001) A ban on asbestos must be based on a comparative risk assessment. Canadian
787 Medical Association Journal, 164, 491-494.
788 Carbone, M., Adusumilli, P.S., Alexander H.R. Jr., Baas, P., Bardelli, F., Bononi, A., Bueno, R.,
789 Felley-Bosco, E., Galateu-Salle, F., Jablons, D., and others. 2019. Mesothelioma: Scientific clues for
790 prevention, diagnosis, and therapy. CA: A Cancer Journal for Clinicians 69, 402-429.
791 Cattaneo, A, Gualtieri, A.F., and Artioli, G. (2003) Kinetic study of the dehydroxylation of chrysotile
792 asbestos with temperature by in situ XRPD. Physics and Chemistry of Minerals, 30, 177-83.
793 Cavallo, A., and Petriglieri, R.J. (2020) Naturally Occurring Asbestos in Valmalenco (Central Alps,
794 Northern Italy): From Quarries and Mines to Stream Sediments. Environmental and Engineering
795 Geoscience, 26, 47–52.
796 Cavariani, F., Marconi, A., and Sala, O. (2010) Asbestos: sampling, analytical techniques and limit
797 values. Italian Journal of Occupational and Environmental Hygiene, 1, 18-28.
798 Chukanov, N.V., Aksenov, S.M., Kasatkin, A.V., Skoda, R., Nestola, F., Nodari, L., Ryanskaya, A.D.,
799 and Rastsvetaeva, R.K. (2019) 3T polytype of an iron-rich oxyphlogopite from the Bartoy volcanic
800 field, Transbaikalia: Mössbauer, infrared, Raman spectroscopy, and crystal structure. Physics and
801 Chemistry of Minerals, 46, 899–908.
802 Churg, A. (1993) Asbestos lung burden and disease patterns in man. In: G.D. Guthrie and Mossmann,
803 B.T., Eds., Health Effects of Mineral Dust, 28, p. 409-426. Reviews in Mineralogical Society of
804 America, Mineralogical Society of America, Chantilly, Virginia.
805 Cogulu, E., and Laurent, R. (1984) Mineralogical and chemical variations in chrysotile veins and
806 peridotite host-rocks from the asbestos belt of southern Quebec. The Canadian Mineralogist, 22,
807 173-183.
808 Collegium Ramazzini (2010) Asbestos is still with us: repeat call for a universal ban. Archives of
809 Environmental and Occupational Health, 65, 121-126.
810 Della Ventura, G. (2017) The analysis of asbestos minerals using vibrational spectroscopies (FTIR,
811 Raman): crystal-chemistry, identification and environmental applications. In A.F. Gualtieri, Ed.,
812 Mineral Fibres: Crystal Chemistry, Chemical-Physical Properties, Biological Interaction and
813 Toxicity, 18, p. 135-169. EMU Notes in Mineralogy, European Mineralogical Union, London.

814 Deng, Z.J., Liang, M.L., Tóth, I., Monteiro, M.J., and Michin, R.F. (2012) Molecular interaction of
815 poly (acrylic acid) gold nanoparticles with human fibrinogen. ACS Nano, 6, 8962-8969.
816 Di Giuseppe, D., Tessari, U., Faccini, B., and Coltorti, M. (2014) The use of particle density in
817 sedimentary provenance studies: the superficial sediment of Po Plain (Italy) case study. Geosciences
818 Journal, 18, 449-458.
819 Di Giuseppe, D., Harper, M., Bailey, M., Erskine, B., Della Ventura, G., Ardith, M., Pasquali, L.,
820 Tomaino, G., Ray, R., Mason, H., and others. (2019) Characterization and assessment of the
821 potential toxicity/pathogenicity of fibrous glaucophane. Environmental Research, 178, 108723.
822 Doll, R. (1955) Mortality from lung cancer in asbestos workers. British Journal of Industrial Medicine,
823 12, 81-86.
824 Donaldson, K., Murphy, F.A., Duffin, R., and Poland, C.A. (2010) Asbestos, carbon nanotubes and the
825 pleural mesothelium: a review of the hypothesis regarding the role of long fibre retention in the
826 parietal pleura, inflammation and mesothelioma. Particle and Fibre Toxicology, 7, 5.
827 French, C.A. (2009) Respiratory tract. In E.S. Cibas, and B.S. Ducatman, Eds., Cytology: Diagnostic
828 principles and clinical correlates, p. 65-103. Elsevier Saunders, Philadelphia, U.S.A.
829 Frost, R.L., and Erickson, K.L. (2004) Thermal decomposition of synthetic hydrotalcites reevesite and
830 pyroaurite. Journal of Thermal Analysis and Calorimetry, 76, 217-225.
831 Gallagher, P.K., and Warne, S.St.J. (1981) Thermomagnetometry and thermal decomposition of
832 siderite. Thermochimica Acta, 43, 253-267.
833 Gannoun, A., Tessalina, S., Bourdon, B., Orgeval, J.J., Birck, J. L., and Allègre, C.J. (2003) Re-Os
834 isotopic constraints on the genesis and evolution of the Dergamish and Ivanovka Cu (Co, Au)
835 massive sulphide deposits, south Urals, Russia. Chemical Geology, 196, 193-207.
836 Garuti, G., Pushkarev, E.V., Thalhammer, O.A., and Zaccarini, F. (2012) Chromitites of the Urals (part
837 1): overview of chromite mineral chemistry and geo-tectonic setting. Ofioliti, 37, 27-53.
838 Gonda, I., and Abd El Khalik, A.F. (1985) On the calculation of aerodynamic diameters of fibers.
839 Aerosol Science and Technology, 4, 233-238.
840 Grosvenor, A.P., Kobe, B.A., Biesinger, M.C., and McIntyre, N.S. (2004) Investigation of multiplet
841 splitting of Fe 2p XPS spectra and bonding in iron compounds. Surface and Interface Analysis, 36,
842 1564–1574.
843 Gualtieri, A.F. (2012) Mineral fibre-based building materials and their health hazards. In F., Pacheco-
844 Torgal, S., Jalali, A. Fucic, Eds., Toxicity of Building Materials, p. 166-195. Woodhead,
845 Cambridge, U.K.

Gualtieri, A.F. (2017) Mineral Fibres: Crystal Chemistry, Chemical-Physical Properties, Biological Interaction and Toxicity, 536 p. European Mineralogical Union, London, U.K.

Gualtieri, A.F. (2018) Towards a quantitative model to predict the toxicity/pathogenicity potential of mineral fibers. Toxicology and Applied Pharmacology, 361, 89-98.

Gualtieri, A.F., Mossman, B.T., and Roggli, V.L. (2017) Towards a general model for predicting the toxicity and pathogenicity of minerals fibres. In A.F. Gualtieri, Ed., Mineral Fibres: Crystal Chemistry, Chemical-Physical Properties, Biological Interaction and Toxicity, 18, p. 501-526.EMU Notes in Mineralogy, European Mineralogical Union, London.

Gualtieri, A. F., Gandolfi, N. B., Pollastri, S., Rinaldi, R., Sala, O., Martinelli, G., Bacci, T., Paoli, F., Viani, A., and Vigliaturo, R. (2018a) Assessment of the potential hazard represented by natural raw materials containing mineral fibres-The case of the feldspar from Orani, Sardinia (Italy). Journal of Hazardous Materials, 350, 76-87.

Gualtieri, A.F., Pollastri, S., Bursi Gandolfi, N., and Lassinantti Gualtieri, M. (2018b) *In vitro* acellular dissolution of mineral fibres: A comparative study. Scientific Reports, 8, 87071.

Gualtieri, A.F., Lusvardi, G., Pedone, A., Di Giuseppe, D., Zoboli, A., Mucci, A., Zambon, A., Filaferro, M., Vitale, G., Benassi, M., and others. (2019a) Structure Model and Toxicity of the Product of Biodissolution of Chrysotile Asbestos in the Lungs. Chemical Research in Toxicology, 32, 2063-2077.

Gualtieri, A.F., Lusvardi, G., Zoboli, A., Di Giuseppe, D., and Lassinantti Gualtieri, M. (2019b) Biodurability and release of metals during the dissolution of chrysotile, crocidolite and fibrous erionite. Environmental Research, 171, 550-557.

Gualtieri, A.F., Andreozzi, G.B., Tomatis, M., and Turci, F. (2019c) Iron from a geochemical viewpoint. Understanding toxicity/pathogenicity mechanisms in iron-bearing minerals with a special attention to mineral fibers. Free Radical Biology and Medicine, 133, 21-37.

Gunter, M.E., Sanchez, M.S., and Williams, T.J. (2007) Characterization of chrysotile samples for the presence of amphiboles: the Carey Canadian Deposit, southeastern Quebec, Canada. The Canadian Mineralogist, 45, 263-280.

Heyder, J., Gebhart, J., Rudolf, G., Schiller, C. F., and Stahlhofen, W. (1986) Deposition of particles in the human respiratory tract in the size range 0.005–15 μm. Journal of Aerosol Science, 17, 811-825.

Hofmeister, A.M., and Bowey, J.E. (2006) Quantitative infrared spectra of hydrosilicates and related minerals. Monthly Notices of the Royal Astronomical Society, 367, 577-591.

878 Holm, N.G., Oze, C., Mousis, O., Waite, J.H., and Guilbert-Lepoutre, A. (2015) Serpentinization and
879 the formation of H_2 and CH_4 on celestial bodies (planets, moons, comets). Astrobiology, 15, 587-
880 600.
881 Hume, L.A., and Rimstidt, J.D. (1992) The biodurability of chrysotile asbestos. American
882 Mineralogist, 77, 1125-1128.
883 IARC (2012) Arsenic, Metals, Fibres and Dust. 100c, 469 p. International Agency for Research on
884 Cancer (IARC), Lyon.
885 IBAS (2020) Current Asbestos Bans. [Online]. Available:
886 http://www.ibasecretariat.org/alpha_ban_list.php [accessed 2020 March 14]. International Ban
887 Asbestos Secretariat (IBAS).
888 ICDD (2020) International Centre for Diffraction Data. [Online]. Available: http://www. icdd.com
889 [accessed 2020 March 14].
890 Ilgren, E.B., Van Orden, D.R., Lee, R.J., Kamiya, Y.M., and Hoskins, J.A. (2015) Further Studies of
891 Bolivian Crocidolite -Part IV: Fibre Width, Fibre Drift and their relation to Mesothelioma Induction:
892 Preliminary Findings. Epidemiology, Biostatistics and Public Health, 12, 1-11.
893 Ivanov, S.N., and Rusin, A.I. (1986) Model for the evolution of the linear fold belt in the continents:
894 example of the Urals. Tectonophysics, 127, 383-397.
895 Ivanov, K.S., Puchkov, V.N., Fyodorov, Y.N., Erokhin, Y.V., and Pogromskaya, O.E. (2013) Tectonics
896 of the Urals and adjacent part of the West-Siberian platform basement: main features of geology and
897 development. Journal of Asian Earth Sciences, 72, 12-24.
898 Jaurand, M.C., Baillif, P., Thomassin, J.H., Magne, L., and Touray, J.C. (1983) X-ray photoelectron
899 spectroscopy and chemical study of the adsorption of biological molecules on chrysotile asbestos
900 surface. Journal of Colloid and Interface Science, 95, 1-9.
901 Jolicoeur, C., and Duchesne, D. (1981) Infrared and thermogravimetric studies of the thermal
902 degradation of chrysotile asbestos fibers: evidence for matrix effects. Canadian Journal of
903 Chemistry, 59, 1521-1526.
904 Kanarek, M.S. (2011) Mesothelioma from chrysotile asbestos: update. Annals of Epidemiology, 21,
905 688-697.
906 Kashansky, S.V., Domnin, S.G., Kochelayev, V.A., Monakhov, D.D., and Kogan, F.M. (2001)
907 Retrospective view of airborne dust levels in workplace of a chrysotile mine in Ural, Russia.
908 Industrial Health, 39, 51-56.

Khilyas, I.V., Sorokina, A.V., Elistratova, A.A., Markelova, M.I., Siniagina, M.N., Sharipova, M.R., Shcherbakova, T.A., D'Errico, M.E., and Cohen, M.F. (2019) Microbial diversity and mineral composition of weathered serpentine rock of the Khalilovsky massif. PloS One, 14, e0225929.

Khorami, J., Choquette, D., Kimmerle, F.M., and Gallagher, P.K. (1984) Interpretation of EGA and DTG analyses of chrysotile asbestos. Thermochima Acta, 76, 87-96.

Kissinger, H.E. (1957) Reaction kinetics in differential thermal analysis. Analytical Chemistry, 29, 1702-1706.

Kohyama, N, Shinohama, Y, and Suzuki, Y. (1996) Mineral phases and some re-examined characteristics of the International Union Against Cancer standard asbestos samples. American Journal of Industrial Medicine, 30, 515-28.

Kovalevskiy, E.V., Schonfeld, S.J., Feletto, E., Moissonnier, M., Kashanskiy, S.V., Bukhtiyarov, I.V., and Schüz, J. (2016) Comparison of mortality in Asbest city and the Sverdlovsk region in the Russian Federation: 1997–2010. Environmental Health, 15, 42.

LaDou, J. (2004). The asbestos cancer epidemic. Environmental health perspectives, 112, 285-290.

Lagarec, K., and Rancourt, D.G. (1998) RECOIL, Mössbauer Spectral Analysis Software for Windows (version 1.0). Department of Physics, University of Ottawa, Canada.

Long, G.J., Cranshaw, T.E., and Longworth, G. (1983) The ideal Mössbauer effect absorber thickness. Mössbauer Effect Reference Data Journal, 6, 42-49.

Marques, M.R., Loebenberg, R., and Almukainzi, M. (2011) Simulated biological fluids with possible application in dissolution testing. Dissolution Technologies, 18, 15-28.

Marsili, D. (2007) Salute e sviluppo: il caso dell'amianto nei Paesi in via di sviluppo, 94 p. Istituto Superiore di Sanità, Roma. (in Italian)

McIntyre, N.S., and Zetaruk, D.G. (1977) X-ray photoelectron spectroscopic studies of iron oxides. Analytical Chemistry, 49, 1521-1529.

Mossman, B.T., and Gualtieri, A.F. (2020) Lung Cancer: Mechanisms of Carcinogenesis by Asbestos. In S. Anttila, P. Boffetta, Eds., Occupational Cancers, p. 239-256. Springer, Heidelberg, Germany.

Münterer, O., and Hermann, J. (1996) The Val Malenco lower crust-man-tle complex and its field relations (Italian Alps). Schweizerische Min-eralogische und Petrographische Mitteilungen, 76, 475-500.

NIOSH (2011) Asbestos fibers and other elongate mineral particles: State of the science and roadmap for research, 62, 153 p. National Institute for Occupational Safety and Health, Cincinnati.

NIMH (2018) ImageJ. [Online]. Available: https://imagej.nih.gov/ij/ [accessed 2020 March 14]. National Institute of Mental Health.

Pollastri, S., Gualtieri, A.F., Lassinantti Gualtieri, M., Hanuskova, M., Cavallo, A., and Gaudino, G. (2014) The zeta potential of mineral fibres. Journal of Hazardous Materials, 276, 469-479.

Pollastri, S., D'Acapito, F., Trapananti, A., Colantoni, I., Andreozzi, G.B., and Gualtieri, A.F. (2015) The chemical environment of iron in mineral fibres. A combined X-ray absorption and Mössbauer spectroscopic study. Journal of Hazardous Materials, 298, 282-293.

Pollastri, S., Perchiazzi, N., Lezzerini. M., Plaisier, J.R., Cavallo, A., Dalconi, M.C., Bursi Gandolfi, N., and Gualtieri, A.F. (2016a) The crystal structure of mineral fibres. 1. Chrysotile. Periodico di Mineralgia, 85, 249-259.

Pollastri, S., Gualtieri, A.F., Vigliaturo, R., Ignatyev, K., Strafella, E., Pugnaloni, A., Croce, A. (2016b) Stability of mineral fibres in contact with human cell cultures. An in situ μXANES, μXRD and XRF iron mapping study. Chemosphere, 164, 547-557.

Puchkov, V.N. (2017) General features relating to the occurrence of mineral deposits in the Urals: What, where, when and why. Ore Geology Reviews, 85, 4-29.

Ristić, M., Czakó-Nagy, I., Musić, S., and Vértes, A. (2011) Spectroscopic characterization of chrysotile asbestos from different regions. Journal of Molecular Structure, 993, 120–126.

Rivero Crespo, M.A., Pereira Gómez, D., Villa García, M.V., Gallardo Amores, J.M., and Sánchez Escribano, V. (2019) Characterization of serpentines from different regions by transmission electron microscopy, X-ray diffraction, BET specific surface area and vibrational and electronic spectroscopy. Fibers, 7, 47.

Rodrigues, E.C., Vallejo, A.C., Ionashiro, E.Y., Bannach, G., and Ionashiro, M. (2005) Synthesis, characterization and thermal behaviour of solid state compounds of 4-methoxybenzoate with Manganese, Nickel and Copper. Eclética Química, 30, 15-20.

Ross, M., and Nolan, R.P. (2003) History of asbestos discovery and use and asbestos-related disease in context with the occurrence of asbestos within ophiolite complexes. In Y., Dilek, S., Newcomb, Eds., Ophiolite concept and the evolution of geological thought, pp. 447-470. Geological Society of America, New York, U.S.A.

Schüz, J., Schonfeld, S.J., Kromhout, H., Straif, K., Kashanskiy, S.V., Kovalevskiy, E.V., Bukhtiyarov, I.V., and McCormack, V. (2013) A retrospective cohort study of cancer mortality in employees of a Russian chrysotile asbestos mine and mills: study rationale and key features. Cancer Epidemiology, 37, 440-445.

Schüz, J., Bukhtiyarov, I., Olsson, A., Moissonnier, M., Ostroumova, E., Feletto, E., Schonfeld, S.J., Byrnes, G., Tskhomariia, I., McCormack, V., and others (2020) Occupational cohort study of current and former workers exposed to chrysotile in mine and processing facilities in Asbest, the Russian Federation: Cohort profile of the Asbest Chrysotile Cohort study. PLoS ONE, 15, e0236475.

Shahgedanova, M. (2003) The physical geography of northern Eurasia, 571 p. Oxford University Press, Oxford.

Siivola, J., and Schmid, R. (2007) A systematic nomenclature for metamorphic rocks: 12. List of mineral abbreviations. Recommendations by the International Union of Geological Sciences (IUGS) Subcommission on the Systematics of Metamorphic Rocks. Recommendations, web version of 01.02.2007.

Sprynskyy, M., NiedojadŁo, J., and Buszewski, B. (2011) Structural features of natural and acids modified chrysotile nanotubes. Journal of Physics and Chemistry of Solids, 72, 1015-1026.

Stanton, M.F., Layard, M., Tegeris, A., Miller, E., May, M., Morgan, E., and Smith, A. (1981) Relation of particle dimension to carcinogenicity in amphibole asbestoses and other fibrous minerals. Journal of National Cancer Institute, 67, 965-975.

Studer, A.M., Limbach, L.K., Van Duc, L., Krumeich, F., Athanassiou, E.K., Gerber, L.C., Moch, H., Stark, W.J. 2010. Nanoparticle cytotoxicity depends on intracellular solubility: comparison of stabilized copper metal and degradable copper oxide nanoparticles. Toxicology Letters, 197, 169-174.

Thomassin, J.H., Goni, J., Baillif, P., Touray, J.C., and Jaurand, M.C. (1977) An XPS study of the dissolution kinetics of chrysotile in 0.1 N oxalic acid at different temperatures. Physics and Chemistry of Minerals, 1, 385-398.

Timbrell, V., Gibson, J.C., and Webster, I. (1968) UICC standard reference samples of asbestos. International Journal of Cancer, 3, 406-408.

Tossavainen, A., Kovalevsky, E., Vanhala, E., and Tuomi, T. (2000) Pulmonary mineral fibers after occupational and environmental exposure to asbestos in the Russian chrysotile industry. American Journal of Industrial Medicine, 37, 327-333.

Tóth, G., Hermann, T., Da Silva, M.R., and Montanarella, L. (2016) Heavy metals in agricultural soils of the European Union with implications for food safety. Environment International, 88, 299-309.

Tylee, B.E., Davies, L.S.T., and Addison, J. (1996) Asbestos reference standards-made available for analysts. Annals of Occupational Hygiene, 40, 711-714.

USGS (2020) Asbestos Statistics and Information. [Online]. Available: https://pubs.usgs.gov/periodicals/mcs2020/mcs2020-asbestos.pdf [accessed 2020 March 14]. United States Geological Service, U.S.A.

Vágvölgyi, V., Kovács, J., Horváth, E., Kristóf, J., and Makó, É. (2008) Investigation of mechanochemically modified kaolinite surfaces by thermoanalytical and spectroscopic methods. Journal of Colloid and Interface Science, 317, 523-529.

Vandenberghe, R.E., Nedkov, I., Merodiiska, T., and Slavov, L. (2005) Surface oxidation control of nanosized magnetite and Mössbauer measurements. Hyperfine Interactions, 165, 267-271.

Vanoeteren, C., Cornelis, R., and Verbeeck, P. (1986) Evaluation of trace elements in human lung tissue III. Correspondence analysis. Science of the Total Environment, 54, 237-245.

Villieras, F., Yvon, J., Cases, J.M., De Donato, P., Lhote, F., and Baeza, R. (1994) Development of microporosity in clinochlore upon heating. Clays and Clay Minerals, 42, 679-88.

Viti, C. (2010) Serpentine minerals discrimination by thermal analysis. American Mineralogist, 95, 631–8.

Vogel, L. (2005) Asbestos in the world. Newsletter of the Health and Safety Department of the European Trade Union Institute–Research, Education, Health & Safety (ETUI-REHS), 27, 7-21.

Whitney, D.L., and Evans, B.W. Abbreviations for names of rock-forming minerals. American Mineralogist, 95, 185-187.

WHO (2014) Chrysotile asbestos. 44 p. World Health Organization, Geneva.

Yeh, H.C., Phalen, R.F., and Raabe, O.G. (1976) Factors influencing the deposition of inhaled particles. Environmental Health Perspectives, 15, 147-156.

Zaccarini, F., Pushkarev, E., Garuti, G., and Kazakov, I. (2016) Platinum-group minerals and other accessory phases in chromite deposits of the Alapaevsk ophiolite, central Urals, Russia. Minerals, 6, 108.

Zucchetti, S., Mastrangelo, F., Rossetti, P., and Sandrone, R. (1988) Serpentinization and metamorphism: their relationships with metallogeny in some ophiolitic ultramafics from the Alps. Proceedings of the Zuffar' Days Symposium in Honor of Piero Zuffardi, p. 137–159. University of Cagliari, Cagliari.

Figures captions

Figure 1. (**a**) Sketch map of the Ural Mountains area. Urals are highlighted with grey color. Map modified after Shahgedanova (2003). (**b**) Simplified geological map of the Urals geotectonic units. For detailed information see section 2.1. Map modified after Puchkov (2017). (**c**) Close-up of dotted square grey shown in (**b**). Map shows the distribution of ophiolites of the southern Urals. Ophiolite complexes are highlighted with black color. Ophiolite complex exploited by Yasniy mine is highlighted with grey circle. Modified after Zaccarini et al. (2016).

Figure 2. X-ray powder diffraction pattern of the sample showing the acronyms of the identified phases and their abbreviations (Siivola and Schmid 2007; Whitney and Evans 2010). The Miller indices of the diagnostic peaks of clinochrysotile are also reported. Owing to the complexity of the pattern, only relevant reflections are labelled. Legend: Ctl = clinochrysotile (00-043-0662 JCPDS card) (major) and ortho-chrysotile (00-052-1563 JCPDS card) (minor); Liz = lizardite 1T (00-050-1625 JCPDS card); Hm = hydromagnesite (00-025-0513 JCPDS card); Mag = magnetite (00-019-0629 JCPDS card). Calcite (00-005-0586 JCPDS card) is also possibly present (major reflection at 29.4 °2θ).

Figure 3. Representative SEM-FEG (**a** and **b**) and STEM (**c** and **d**) images of the Russian chrysotile. The sample is characterized by aggregates of fibrils typically arranged in bundles (**a**, **b**). The bundles exhibit "split-ends" (**b**) and both individual fibrils and bundles can exhibit slight curvature (**a**, **b**). The mean width of fibrils is 40 nm (**c**, **d**). Magnetite particles are evident within the chrysotile bundles (**c**, **d**).

Figure 4. Chrysotile fibers observed with PCOM showing the typical colors obtained with the 1.550 refractive index liquid. Mineral fibers observed with PCOM in bright field (**a**) and (**b**); dark field (**c**) and (**b**). Fibers parallel to the polarizer, in bright field, have blue color and orange halo (**a**); fibers perpendicular to the polarizer, in bright field, have pale blue color and orange halo (**b**); Fibers parallel to the polarizer, in dark field, have purple color fibers (**c**); fibers perpendicular to the polarizer, in dark field, have blue color (**d**).

1065 **Figure 5.** Zeta potential versus pH curves. (**a**) Russian chrysotile in double-distilled water and ALF
1066 solution. (**b**) Yasniy chrysotile (solid line) and UICC chrysotile (dashed line) in both double-distilled
1067 water and ALF solution.
1068
1069 **Figure 6.** Thermal analyses (TG, DTG and DTA) and evolved gas mass spectrometry (MS-EGA) of
1070 the sample before (**a** and **b**) and after (**c** and **d**) the treatment with ethyl acetate.
1071
1072 **Figure 7.** FPTI calculated for Russian chrysotile and other mineral fiber species.

Figure 1

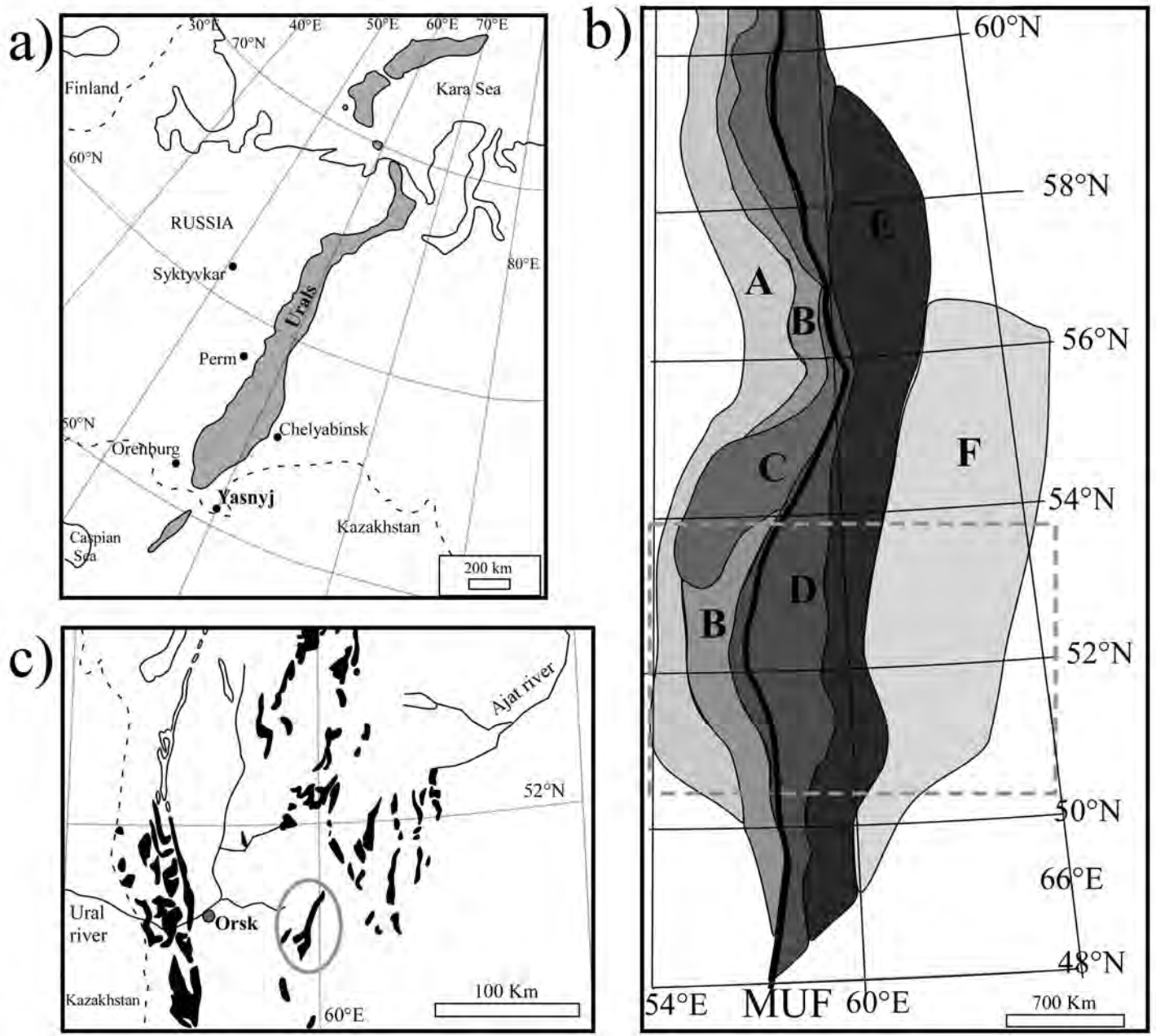
a)
30°E
40°E
50°E
60°E
70°E
70°N
Finland
Kara Sea
60°N
RUSSIA
80°E
Syktyvkar
Urals
Perm
50°N
Chelyabinsk
Orenburg
Yasnyj
Kazakhstan
Caspian Sea
200 km
b)
60°N
58°N
56°N
54°N
52°N
50°N
A
B
C
D
E
F
66°E
48°N
54°E
MUF
60°E
700 Km
c)
Ajat river
52°N
Ural river
Orsk
Kazakhstan
60°E
100 Km

Figure 2

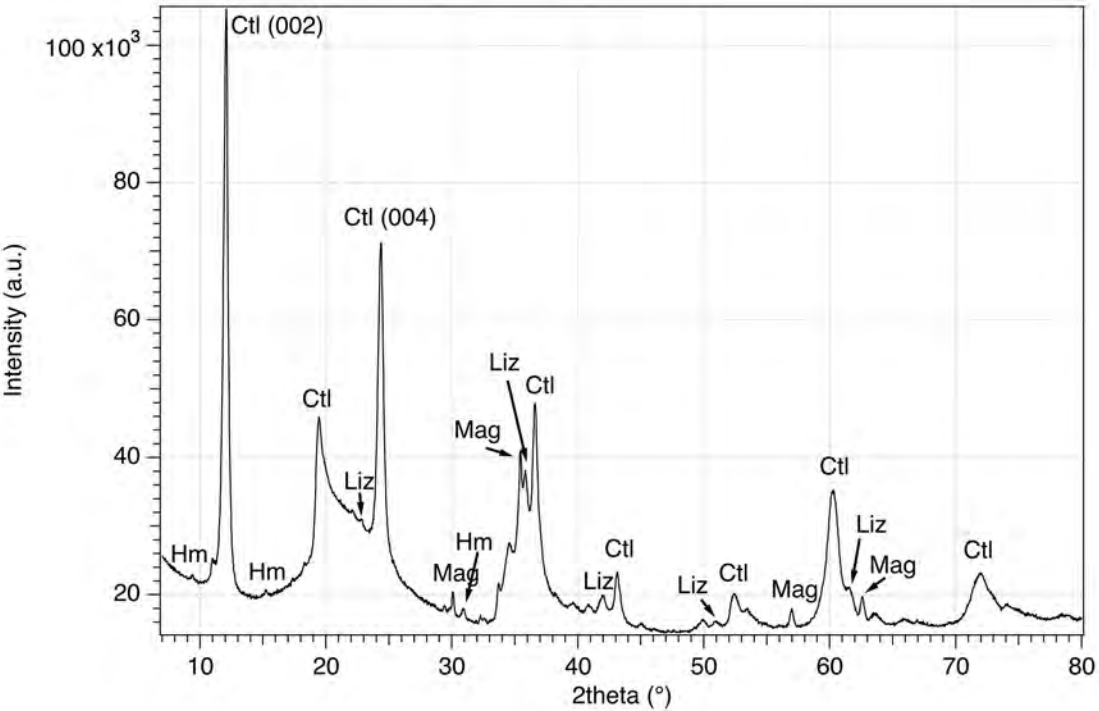
Ctl (002)
Ctl (004)
Ctl
Liz
Mag
Hm
Intensity (a.u.)
100 x10^3
80
60
40
20
10
20
30
40
50
60
70
80
2theta (°)

Figure 3

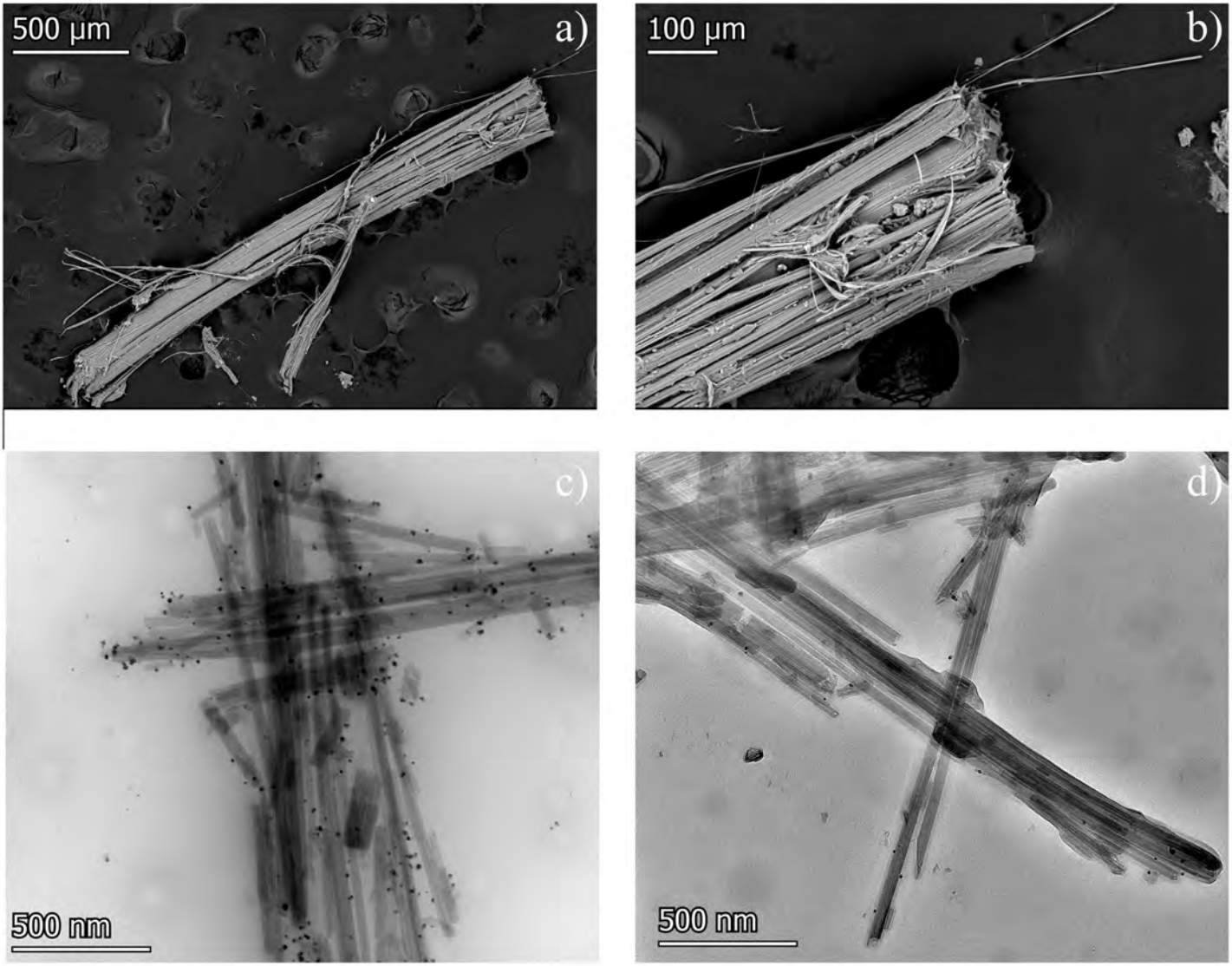

Figure 4

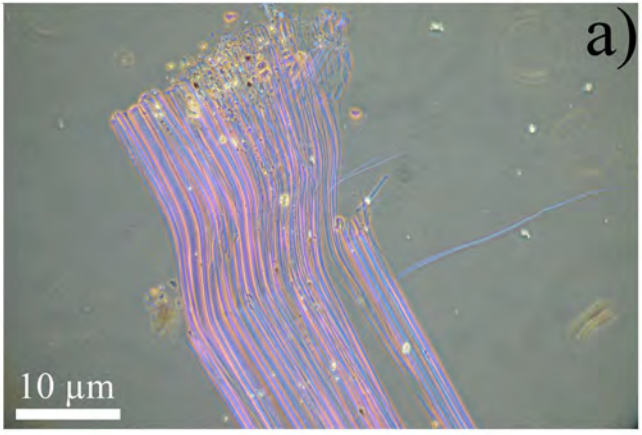

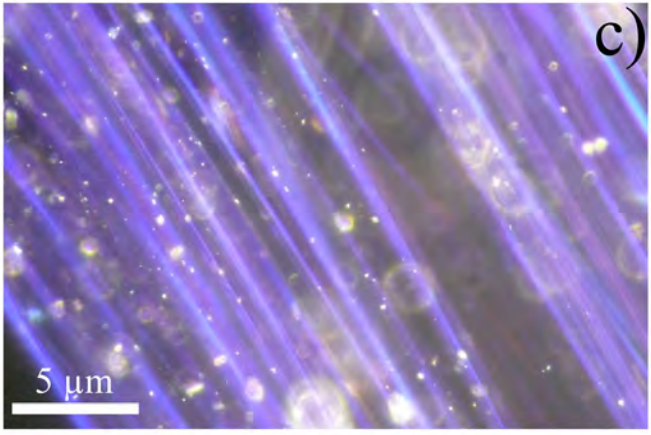

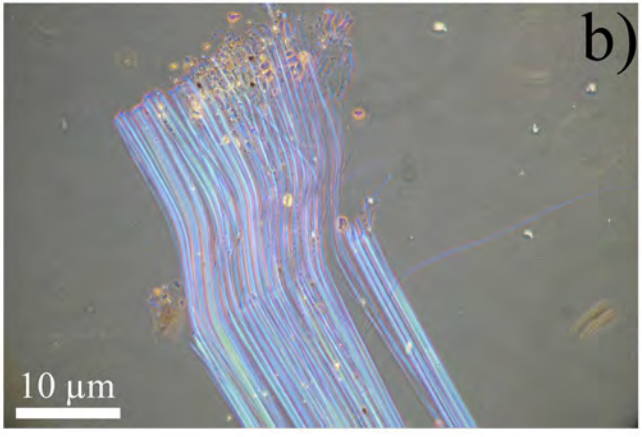

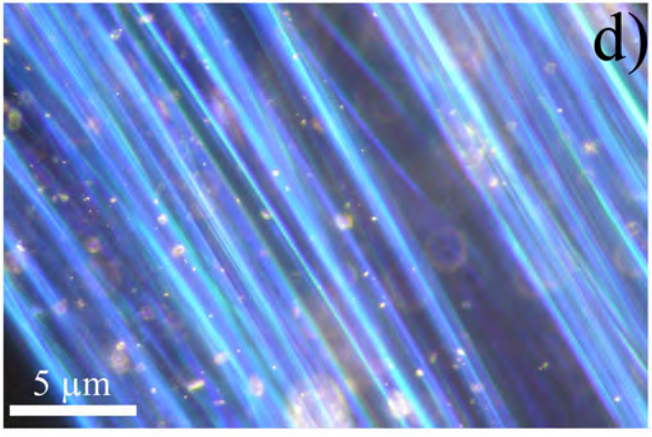

Figure 5

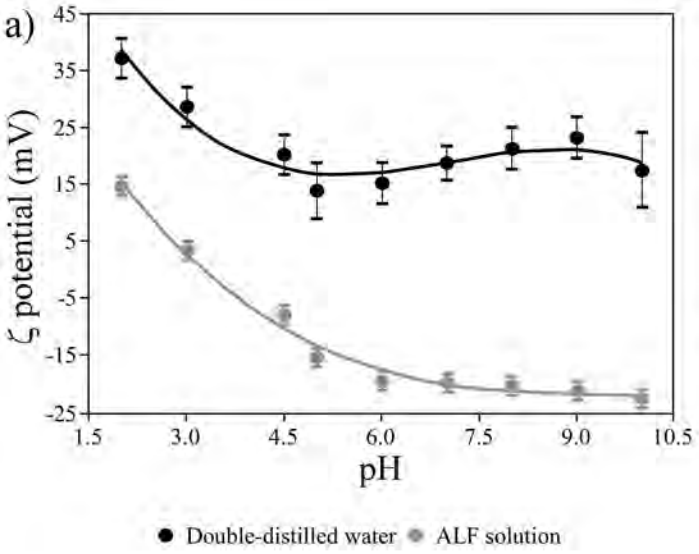
a)
ζ potential (mV)
45
35
25
15
5
-5
-15
-25
1.5
3.0
4.5
6.0
7.5
9.0
10.5
pH
Double-distilled water
ALF solution

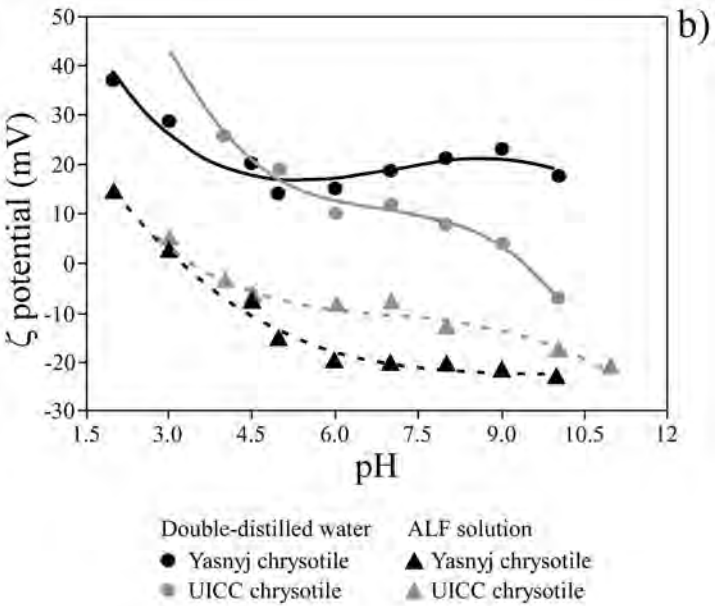
b)
ζ potential (mV)
50
40
30
20
10
0
-10
-20
-30
1.5
3.0
4.5
6.0
7.5
9.0
10.5
12
pH
Double-distilled water
Yasnyj chrysotile
UICC chrysotile
ALF solution
Yasnyj chrysotile
UICC chrysotile

Figure 6

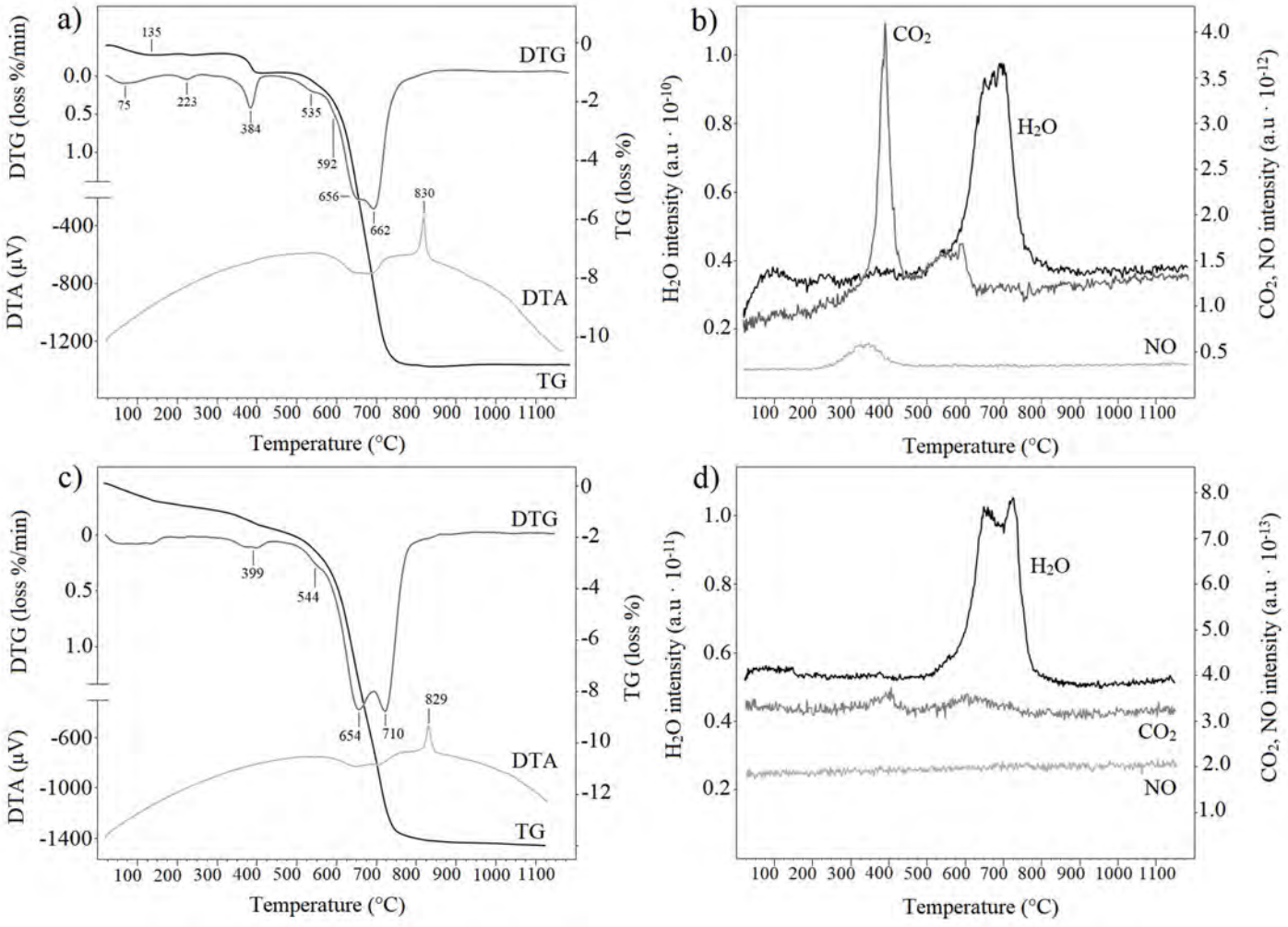
a)
DTG (loss %/min)
DTA (μV)
TG (loss %)
DTG
DTA
TG
135
75
223
384
535
592
656
662
830
Temperature (°C)
b)
H_2O intensity (a.u · 10^{-10})
CO_2, NO intensity (a.u · 10^{-12})
CO_2
H_2O
NO
Temperature (°C)
c)
DTG (loss %/min)
DTA (μV)
TG (loss %)
DTG
DTA
TG
399
544
654
710
829
Temperature (°C)
d)
H_2O intensity (a.u · 10^{-11})
CO_2, NO intensity (a.u · 10^{-13})
H_2O
CO_2
NO
Temperature (°C)

Figure 7

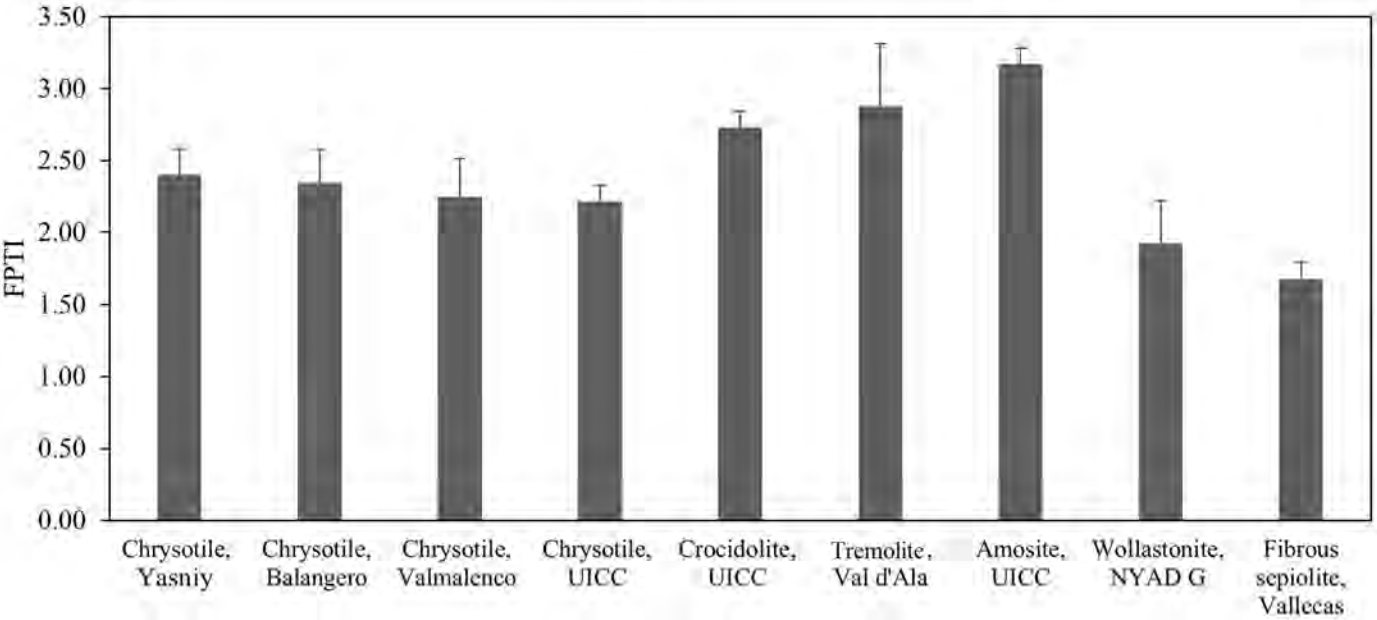
3.50
3.00
2.50
2.00
1.50
1.00
0.50
0.00
FPTI
Chrysotile, Yasniy
Chrysotile, Balangero
Chrysotile, Valmalenco
Chrysotile, UICC
Crocidolite, UICC
Tremolite, Val d'Ala
Amosite, UICC
Wollastonite, NYAD G
Fibrous sepiolite, Vallecas

Table 1. The parameters of the FPTI model with the values calculated for the chrysotile from Yasnyj (Russia) (this paper). For comparison the values calculated for other chrysotiles investigated by our group are also reported (Gualtieri 2018).

Parameters	classes	Normalized score $FPTI_i$	Chrysotile, Yasniy (Russia)	Chrysotile, Balangero (Italy)	Chrysotile Valmalenco (Italy)	Chrysotile UICC (Canada)
(1,1) Length	>5μm and <10μm	0.10	0.40	0.40	0.20	0.40
	>10μm and <20μm	0.20				
	>20μm	0.40				
(1,2) Diameter	>1μm and <3μm	0.10	0.20	0.10	0.20	0.20
	>0.25μm and <1μm	0.20				
	>0.25μm	0.40				
(1,3) Crystal curvature	Flat surface (perfect	0.05	0.20	0.20	0.20	0.20
	crystal)	0.10				
	Altered surface	0.20				
	Cylindrical surface					
(1,4) Crystal habit	Curled	0.10	0.10	0.10	0.10	0.10
	Mixed Curled/acicular	0.20				
	Acicular	0.40				
(1,5) Fiber density	<2.75 $g \cdot cm^{-3}$	0.05	0.05	0.05	0.05	0.05
	>2.75 and <3.5 $g \cdot cm^{-3}$	0.10				
	>3.5 $g \cdot cm^{-3}$	0.20				
(1,6) Hydrophobic character	Hydrophobic	0.05	0.20	0.20	0.20	0.20
of the surface	Amphiphilic	0.10				
	hydrophilic	0.20				
(1,7) Surface area	>25 m^2g^{-1}	0.05	0.10	0.05	0.05	0.05
	<25 and > 5 m^2g^{-1}	0.10				
	<5 m^2g^{-1}	0.20				
(1,8) Total iron content	Fe_2O_3+FeO wt% <1	0.05	0.10	0.10	0.10	0.10
	1 < Fe_2O_3+FeO wt% < 10	0.1				
	Fe_2O_3+FeO wt% > 10	0.2				
(1,9) Ferrous iron	0 < FeO wt% < 0.25	0.05	0.10	0.20	0.20	0.20
	0.25 < Fe Owt% < 1	0.10				
	Fe Owt% > 1	0.20				
(1,10) Surface ferrous	Fe^{2+} nuclearity > 2	0.02	0.033	0.033	0.033	0.033
iron/iron nuclearity	Fe^{2+} nuclearity = 2	0.03				
	Fe^{2+} nuclearity = 1	0.07				
(1,11) Content of metals other than iron*	$\sum_i \frac{C_i}{L_i} < 1$	0.10	0.40	0.40	0.40	0.20
	$1 < \sum_i \frac{C_i}{L_i} < 5$	0.20				
	$\sum_i \frac{C_i}{L_i} > 5$	0.40				

(1,12) Dissolution rate log(R)**	<1y	0.05	0.05	0.05	0.05	0.05
	>1 and <40y	0.10				
	>40y	0.20				
(1,13) Velocity of iron release***	<0.1	0.033	0.133	0.133	0.133	0.133
	>0.1 and <1	0.067				
	>1	0.133				
(1,14) Velocity of silica dissolution****	<0.5	0.016	0.067	0.067	0.067	0.067
	>0.5 and <1	0.033				
	>1	0.067				
(1,15) Velocity of release of metals*****	<1	0.033	0.133	0.133	0.133	0.067
	>1 and <10	0.067				
	>10	0.133				
(1,16) Zeta potential (ς)	Negative at pH=4.5	0.10	0.10	0.10	0.10	0.10
	Negative at both pH=4.5 and 7	0.20				
(1,17) Fibers' aggregation	ς>|20|	0.033	0.033	0.033	0.033	0.067
	|10|<ς<|20|	0.066				
	|0|<ς<|10|	0.133				
(1,18) Cation exchange (in zeolites)	cation Exchange	0.067	0.0	0.0	0.0	0.0
	no cation exchange	0.0				
		FPTI (error)	2.40 (0.18)	2.35 (0.22)	2.25 (0.26)	2.22 (0.28)

* $\sum_i \frac{C_i}{L_i}$ =sum of the concentrations of heavy metals (Sb, As, Hg, Cd, Co, Cr, Cu, Pb, Ni, Zn, V, Be) C_i in the fiber (ppm) divided by the limit L_i for that metal according to the existing regulatory system (see Table 6) except for Be with limit = 0.5 $mg \cdot kg^{-1}$; **the total dissolution time of the fiber calculated in years (y) following the standardized acellular *in vitro* dissolution model at pH=4.5 described in reference (Gualtieri et al. 2018b); ***total content of elemental iron in the fiber (wt%) possibly made available as active iron at the surface of the fiber divided by the total dissolution time (y) of the fiber (see Table 4); ****total content of Si of the fiber (wt%) divided by the total dissolution time (y) of the fiber; *****total content (ppm) of metals and potentially toxic elements (i.e., Sb, As, Be, Cd, Co, Cr, Cu, Pb, Mn, Ni, Zn and V) divided by the total dissolution time (y) of the fiber.

Table 2. Summary statistics of the geometry of Russian chrysotile fibers. L (length); W (width); Min (minimum); Max (maximum); σ (standard deviation).

		Percentiles						
	Min	5th	25th	50th	75th	95th	Max	σ
L (μm)	1.36	3.90	15.1	27.2	45.3	81.9	188	28.2
W (μm)	0.05	0.10	0.37	0.59	0.80	1.65	2.79	0.46

Table 3. The optical properties of Russian chrysotile.

Property	Values
Color	White, pale green
Pleochroism	Weak
Optic Sign	Biaxial (-)
2V	30°
Birefringence	I Order 0.001-0.010
Extinction	Parallel to fibers (undulate)
Sign of elongation	Positive
Color fiber parallel dispersion staining* (dark field)	Purple
Color fiber perpendicular dispersion staining (dark field)	Blue
Color fiber parallel phase contrast (bright field)	Blue (orange halo)
Color fiber perpendicular phase contrast (bright field)	Pale blue (orange halo)
Refractive index liquid	1.550

Note: Fiber parallel or fiber perpendicular describes orientation with respect to the polarizer

Table 4. Kinetic parameters calculated for the dissolution of selected mineral fibers. Table contains the specific surface area (SSA), apparent rate constant (k), the apparent dissolution rate (R), and the estimated lifetime (t) of a fiber.

	SSA (m^2g^{-1})	k (s^{-1})	R ($mol \cdot m^{-2}s^{-1}$)	t (days)	t (years)
Yasniy chrysotile	18.4(5)	$2.30(8)\times10^{-10}$	$5.10(7)\times10^{-10}$	129(45)	0.40(1)
Balangero chrysotile	42.0(1)	$1.80(6)\times10^{-10}$	$1.70(6)\times10^{-10}$	124(41)	0.30(1)
UICC chrysotile	43.0(2)	$2.50(7)\times10^{-10}$	$2.30(6)\times10^{-10}$	94.0(26)	0.30(1)
Valmalenco chrysotile	68.0(9)	$2.10(6)\times10^{-10}$	$1.20(3)\times10^{-10}$	177(51)	0.50(1)
UICC amosite	9.50(3)	$6.10(6)\times10^{-14}$	$2.70(3)\times10^{-13}$	27010(2647)	74.0(7)
UICC anthophyllite asbestos	4.40(2)	$1.20(3)\times10^{-13}$	$1.00(3)\times10^{-13}$	83950(20990)	245(64)
Val d'Ala tremolite asbestos	9.20(3)	$5.40(9)\times10^{-14}$	$4.50(7)\times10^{-13}$	17885(2981)	49.0(8)
UICC crocidolite	16.1(6)	$1.30(3)\times10^{-13}$	$3.20(7)\times10^{-13}$	24090(5840)	66.0(16)

Table 5. Calculated Mössbauer hyperfine parameters at 293K, χ^2: 0.98 for the Russian chrysotile.

	δ (mm/s)	Δ (mm/s)	Γ_+ (mm/s)	B (T)	A (%)	Assignment
Doublet 1	1.13±0.03	2.78±0.05	0.23±0.04		17±1	Fe^{2+} octahedral
Doublet 2	0.32±0.05	0.52±0.08	0.41±0.08		28±1	Fe^{3+} octahedral
Sextet 1	0.27±0.02	-0.01±0.01	0.18±0.03	49.4±0.2	21±1	Magnetite site A
Sextet 2	0.63±0.02	0.01±0.01	0.27±0.04	45.9±0.2	34±2	Magnetite site B

Table 6. Trace elements concentration ($mg \cdot kg^{-1}$) of the Russian chrysotile sample, concentration found in the human lungs (Vanoeteren et al. 1986) and threshold values (Tóth et al. 2016); n.a. (not available).

	Russian chrysotile	Elements in human lungs	Threshold values
V	186(9)	0.50	100
Cr	5461(277)	0.50	100
Mn	2305(124)	3.00	n.a.
Co	233(10)	0.01	20.0
Ni	5521(238)	1.00	50.0
Cu	61.6(4)	5.00	100
As	6.51(1)	0.10	5.00
Pb	615(6)	0.50	60.0
Be	3.51(0.1)	0.03	n.a.